Lipid bilayers: Phase behavior and nanomechanics

Lorena Redondo-Morata, Patricia Losada-Pérez, Marina Inés Giannotti

HAL Id: hal-02976730

https://hal.science/hal-02976730

Submitted on 23 Oct 2020

1 Lipid bilayers: phase behavior and

2 nanomechanics

3 **LORENA REDONDO-MORATA**

4 *Center for Infection and Immunity of Lille, INSERM U1019, CNRS UMR 8204, F-59000 Lille, France.*

5 **PATRICIA LOSADA-PÉREZ**

6 *Experimental Soft Matter and Thermal Physics (EST) group, Department of Physics, Université*
7 *Libre de Bruxelles, 1050 Brussels, Belgium*

8 **MARINA INÉS GIANNOTTI**

9 *Biomedical Research Networking Center on Bioengineering, Biomaterials and Nanomedicine*
10 *(CIBER-BBN), Spain.*

11 *Institut de Bioenginyeria de Catalunya (IBEC), The Barcelona Institute of Science and Technology*
12 *(BIST), 08028 Barcelona, Spain.*

13 *Departament de Ciència de Materials i Química Física, Universitat de Barcelona, 08028*
14 *Barcelona, Spain.*

15 *migiannotti@ibecbarcelona.eu*

16

17 ***Keywords:***

18 *Lipid phase behavior / phase transition / phase coexistence / nanomechanics / thermodynamics*
19 */ Atomic Force Microscopy (AFM)/ Quartz crystal microbalance with dissipation monitoring*
20 *(QCM-D)*

21

22 Contents

42

43   1. Abstract

44   Lipid membranes are involved in many physiological processes like recognition, signaling, fusion

45   or remodeling of the cell membrane or some of its internal compartments. Within the cell, they

46   are the ultimate barrier, while maintaining the fluidity or flexibility required for a myriad of

47   processes, including membrane protein assembly. The physical properties of *in vitro* model

48   membranes as model cell membranes have been extensively studied with a variety of

49   techniques, from classical thermodynamics to advanced modern microscopies. Here we review

50   the nanomechanics of solid-supported lipid membranes with a focus in their phase behavior.

51   Relevant information obtained by quartz crystal microbalance with dissipation monitoring

52   (QCM-D) and atomic force microscopy (AFM) as complementary techniques in the

53   nano/mesoscale interface is presented. Membrane morphological and mechanical

54   characterization will be discussed in the framework of its phase behavior, phase transitions and

55   coexistence, in simple and complex models, and upon the presence of cholesterol.

2. Introduction

Cells can be thermodynamically defined as open systems in constant exchange of mass, energy and information with the environment. The membrane is the ultimate boundary for the cell, confining it from the medium and some of its internal compartments. The cell membrane is a fundamental structure of the cell, providing a support matrix for proteins and carbohydrates. As complex systems, cell membrane performance is the result of lipids and proteins working together, with main functions like being barriers, mediating the exchange of molecules and information, promoting signaling and adhesion, and being metabolically self-renewing structures.

Cell membranes are materials with unique physical properties allowing cells to rapidly change shape, squeeze, stretch, pinch off smaller units, fuse, and reseal. This is the result of being viscous sheets with both fluid and elastic properties. Cell membranes are supramolecular structures, where the lipids and proteins interact through non-covalent bonding. Membranes are curved surfaces, vesicular in nature, whose curvature is deeply influenced by the lipid packing. The lipid bilayer, made of millions of building blocks held together by weak interactions, is in part responsible for the physical, dynamic and mechanical properties of the cell membrane. In the membrane, lipids are mainly organized in lamellar phases, where two leaflets of lipids are self-assembled exposing the polar headgroups to the aqueous interface and keeping the fatty-acyl chains aligned opposed and parallel to one another to form the hydrophobic core.

The enterprising scientist Alec Bangham was the discoverer in 1958 of the 'multilamellar smectic mesophases' or, as himself referred to less seriously, the 'bangasomes' (Bangham et al., 1958) - which were eventually named 'liposomes' to define microscopic lipid vesicles (Sessa & Weissmann, 1968). When the Babraham Institute (Cambridge, UK) acquired its first electron microscope in 1961, Bangham had the privilege to firstly observe the dispersions of phospholipids in water solutions of negative stains (Bangham & Horne, 1964). In the following years, Bangham and his collaborators performed the key experiments to demonstrate that lipid bilayers maintain concentration gradients of ions such as potassium and sodium. Indeed, David D. Deamer wrote in his memoir "*It was the membrane equivalent of finding the double helix structure of DNA, another Cambridge discovery in the life sciences*"(Deamer, 2010). This was reflected in the well-known lecture by Bangham in the University of Bristol in 1975, entitled "Membranes came first", where he proposed that something similar to liposomes had been available to house the first forms of life. Indeed, all living organisms have a membrane.

88　　Later in the early 1970s, Singer and Nicolson proposed the fluid-mosaic-model, depicting the

89　　cell membranes as two-dimensional liquids where all lipid and protein molecules diffuse easily

90　　(Singer & Nicolson, 1972). Concerning the composition, besides all the proteins and

91　　carbohydrates, lipids are the main components of the cell membrane in terms of molar fraction.

92　　Lipids are a broad family which covers many different chemical structure sphingolipids

93　　(ceramides, sphingomyelin, gangliosides, sphingosines), sterols (cholesterol and vitamins), and

94　　phospholipids, each of them contributing to different and crucial physicochemical properties.

95　　Gradual progress was made in the knowledge of the complexity of the biological membranes.

96　　The most famous hypothesis in the field is the membrane raft proposed in 1997 by K. Simons

97　　and E. Ikonen (Simons & Ikonen, 1997). The idea was based on the fact that portions of

98　　membrane were found to be detergent resistant, that may give rise to a virtual

99　　compartmentalization of the cell. This hypothesis generated a lot of literature and became a

100　　recursive concept in the field. Nowadays it is well known that there is a variety of nanostructures

101　　in the membrane of heterogeneous sizes and functions, and the methods that allow us to

102　　observe these nanodomains *in vivo* are only beginning to emerge (Goñi, 2019b; Pinkwart et al.,

103　　2019). Nanodomains can be considered putative heterogeneous structures within the

104　　membrane which are due partly to phase separation.

105　　The mechanical role of the lipid membrane in force-triggered and force-sensing mechanisms in

106　　cells is of significance and adds to the better-established role of the mechanosensitive proteins

107　　(Vogel, 2006)(Kechagia et al., 2019). Membrane conformational changes such as bending,

108　　vesiculation or tubulation are involved in cellular processes including adhesion, signaling,

109　　endocytosis or membrane resealing (van Meer & de Kroon, 2011)(van Meer et al.,

110　　2008)(Hassinger et al., 2017). For instance, in endocytosis, the endocytic system needs to

111　　generate enough force to form an endocytic vesicle by bending the membrane. These

112　　mechanisms generally require the membrane separation from the cytoskeleton as well as strong

113　　bending, for which the membrane chemical composition and physicochemical properties, often

114　　highly localized and dynamic, are key players (Sheetz, 2001)(van Meer et al., 2008). It is now

115　　clear that the lipid packing and composition are direct modulators of the membrane curvature

116　　and elasticity, at different scales, even locally at the nanometer scale (Yeagle, 1989)(Vereb et

117　　al., 2003). Understanding the lipid bilayers structural and mechanical properties and the

118　　involvement and role of each individual component turns out to be essential in order to identify

119　　their contribution to the overall membrane traits. Structural and physical properties of lipid

120　　bilayers include shape and local distribution of components (phases and domains), and related

121　　mechanical stability in response to compression, bending or stretching, their ability to fuse, etc.

122   We review the nanomechanics of solid-supported lipid membranes and how these relate to lipid

123   membrane phase behavior. To this end, we chose two complementary techniques with

124   nano/mesoscale sensitivity to mechanical and viscoelastic properties, namely quartz crystal

125   microbalance with dissipation monitoring (QCM-D) and atomic force microscopy (AFM). QCM-D

126   is a label-free surface-sensitive technique, whose working principle is based on the inverse

127   piezoelectric effect. Real-time simultaneous measurements of resonant frequency and energy

128   dissipation make QCM-D very suitable for gravimetric and viscoelastic characterization of solid-

129   supported nanoscale sized films. AFM is a technique that allows the observation of surfaces

130   under controlled liquid environment, to resolve topographical features with nanoscale

131   resolution and to measure and apply forces in the pN-nN range. Therefore, AFM is appropriate

132   for imaging the topography of solid-supported lipid membranes and probing the physical and

133   mechanical properties at the nanoscale by means of force spectroscopy, providing high spatial

134   and force resolution. QCM-D is complementary to AFM, useful for probing changes in

135   viscoelastic properties during solid-supported film formation. The complementarity of AFM and

136   QCM-D manifests at different levels: i) AFM measurements are performed at a local level, while

137   QCM-D provides a global characterization of the solid-supported films; ii) both techniques

138   enable dynamic mechanical analysis by applying a small oscillatory stress, however, the AFM tip

139   scans and deforms supported layers from the top, whereas QCM-D measures the sensor

140   oscillation from the bottom. The combination of AFM and QCM-D for supported lipid

141   membranes has been employed in previous works (see, for instance (R. Richter et al., 2003,

142   2003; Van Lehn et al., 2014). In the following sections we briefly describe the membrane models

143   and discuss the working principles behind both approaches, highlighting the quantitative and

144   qualitative mechanical information that can be extracted using each technique. Specific

145   examples on the usefulness to monitor phase transitions on one-component to more complex

146   bilayers, and resolve domain coexistence are also provided, including the key role of cholesterol.

147   3. Experimental approaches to study membrane mechanics

148   3.1. Model systems: supported vesicles layers (SVLs) lipid bilayers (SLBs)

149   Due to the extreme complexity of biological membranes, cell membrane mimetics are excellent

150   approaches to study membrane properties and biological processes at the cellular and

151   subcellular level. A great deal of what we know about these processes comes from modeling

152   lipid bilayers *in vitro*. Various membrane systems are established as biomimetic structures. They

153   include vesicles: freely-suspended and supported liposomes, giant unilamellar vesicles (GUVs);

154   micelles, bicelles; suspended and supported lipid films: Langmuir monolayers, phospholipid

155   bilayers nanodiscs, black lipid membranes (BLM), supported lipid bilayers (SLB), tethered bilayer

156 lipid membranes (tBLM), polymer-cushioned membranes, protein-tethered bilayer lipid
157 membranes (ptBLM) and hybrid bilayers (Sebaaly et al., 2019)(Dimova, 2019)(Doktorova et al.,
158 2018)(Siontorou et al., 2017)(Rascol et al., 2016). Among these, the giant unilamellar vesicles
159 (GUVs) have been extensively used since they offer a perfect stage to study the mechanical,
160 thermodynamic, electrical, and rheological properties of the overall GUV and lipid bilayer as a
161 function of membrane composition, surrounding media and temperature (Dimova, 2019)(Evan
162 Evans et al., 2003)(Kahya et al., 2004). Being heterogeneous and dynamic at the nanoscale,
163 nanotechnology-based techniques can further explore biomembranes locally with resolution at
164 the nanometric level. For many of these techniques, like surface analytical techniques, solid-
165 supported models are the most adequate, including supported lipid monolayers, supported
166 vesicles layers (SVLs) or supported lipid bilayers (SLBs).

167 SVLs are the precursor solid-supported systems to planar SLBs formed by vesicle fusion and
168 rupture. They result from spontaneous adsorption of small vesicles of diameter d $\leq$ 200 nm onto
169 solid surfaces. The geometry of SVLs embodies membrane curvature, tension and osmotic stress
170 within the supported layer. This makes SVLs useful biomimetic platforms to probe membrane
171 deformation using surface-sensitive techniques and testing ground for adhesion, budding and
172 lipid membrane exchange and fusion (Lipowsky & Seifert, 1991; Hurley et al., 2010; Tabaei et
173 al., 2016; Steinkühler et al., 2019). SVLs are generally formed by small soft adsorbates which are
174 mimics to small endosomes or exosomes. These are optically inaccessible systems and the
175 experimental investigation of their deformation is not straightforward. Adsorbed vesicles onto
176 inorganic surfaces also serve as model systems relevant to biocompatibility studies. Vesicle
177 adsorption is very often accompanied by vesicle deformation upon contact with the solid
178 support. The extent of vesicle deformation depends on several factors such as vesicle size,
179 mechanical properties of the vesicles, adhesion strength of the surface, osmotic pressure
180 difference over the vesicle, etc. The fate of vesicles upon adsorption on a solid support depends
181 both on vesicle-vesicle and vesicle surface interactions. In the absence of osmotic stress and at
182 a concentration where vesicle surface coverage enhances fusion probability, the rupture of
183 vesicles will depend strongly on the adhesion strength. Specifically on how this imbalances the
184 energetic competition between adhesion energy and an elastic stretching of the membrane
185 (Lipowsky & Seifert, 1991). If the adhesion strength W is large enough and exceeds the lysis
186 tension of the membrane, the vesicles will rupture. SVLs are typically formed on surfaces whose
187 adhesion strength is not sufficient to induce vesicle rupture, such as Au, TiO_2, Pt (Tero, 2012).

188 SLBs are very manageable platforms relatively simple to obtain and that retain two-dimensional
189 order and lateral mobility. They are ideal to study lipid lateral interactions and membrane local

190   mechanical properties, growth of lipid domains, as well as interactions between the lipid

191   membrane and proteins, peptides and drugs, cell signaling, etc. They also offer an excellent

192   environment for inserting membrane proteins. There are many different methods that can be

193   used to obtain SLBs, like the spin-coating and hydration (Mennicke & Salditt, 2002),

194   microcontact printing (Strulson & Maurer, 2011), solvent-exchange deposition (Tabaei et al.,

195   2016; Hohner et al., 2010), and the most widely used methods like the Langmuir–

196   Blodgett/Schäfer deposition to prepare mono and bilayers (Kurniawan et al., 2018), and the

197   liposome fusion and rupture method for bilayers (Hardy et al., 2013)(Mingeot-Leclercq et al.,

198   2008). The liposome rupture method remains the most popular and simple one, based on

199   depositing small unilamellar vesicles (SUVs) from a suspension onto a flat substrate where the

200   adhesion strength is high, generally mica or silicon oxide, but can also be formed on bare or

201   gold-coated glass, following the needs of the analysis technique (Mingeot-Leclercq et al., 2008;

202   Ralf P Richter & Brisson, 2005)(Choi et al., 2016; B. Gumí-Audenis et al., 2018; Seeger et al., 2010;

203   Winkler et al., 2020). Once in contact with the substrate the SUVs start fusing between them,

204   deforming, flattening, and finally rupturing to form a continuous film. It is important to have in

205   mind that the final SLB structure is affected by variables like the lipid vesicles composition,

206   concentration, and size, the physicochemical environment pH, temperature, and ionic strength,

207   as well as the surface roughness and charge density (Reimhult et al., 2003).

3.1 QCM-D

209   Quartz crystal microbalance with dissipation monitoring (QCM-D) is an acoustic-based surface-

210   sensitive technique that enables label-free, real-time simultaneous measurements of wet-mass

211   and viscoelastic properties of solid-supported nano/meso-scaled adlayers.

212   The QCM-D sensor consists of an AT-cut quartz crystal being sandwiched between two

213   electrodes. When an AC voltage is applied across the electrodes with a frequency close to the

214   resonant frequency of the quartz crystal, a mechanical deformation is induced, resulting in a

215   standing shear wave. The surfaces of the electrodes coincide with the antinodes of the standing

216   shear wave with wavelength $\lambda = 2d/n$, with d the quartz thickness and n the (odd) overtone

217   number. The resonance frequency at each overtone is $f_n = nv/2d$, with v the speed of sound in

218   quartz. The shear waves propagate as evanescent waves decaying across the boundary between

219   the crystal and the fluid environment (air or liquid) with a penetration depth $\delta = \sqrt{\eta_L / \pi f_n \rho_L}$,

220   which depends on the overtone frequency f_n and on the viscosity η_L and density ρ_L of the fluid in

221   contact with the sensor surface (Reviakine et al., 2011). The penetration depth of a 5 MHz shear

222   wave in water is $\delta \sim 250$ nm, rendering QCM-D surface-specific. D is defined as the ratio

223   between the dissipated energy during one vibration period and the total energy of the crystal at

224   that instant $D = E_{lost} / 2\pi E_{stored}$. In the so-called 'ring-down method' measurements, energy

225   dissipation *D* can be calculated when the AC voltage driving the quartz crystal oscillation is

226   turned off. The working principle of QCM-D is reflected in Figure 1, upon the presence of a soft,

227   viscoelastic layer such as a layer of lipid SVLs. The amplitude of the crystal oscillation decays

228   exponentially and much faster when in contact with a viscoelastic layer, characterized by a large

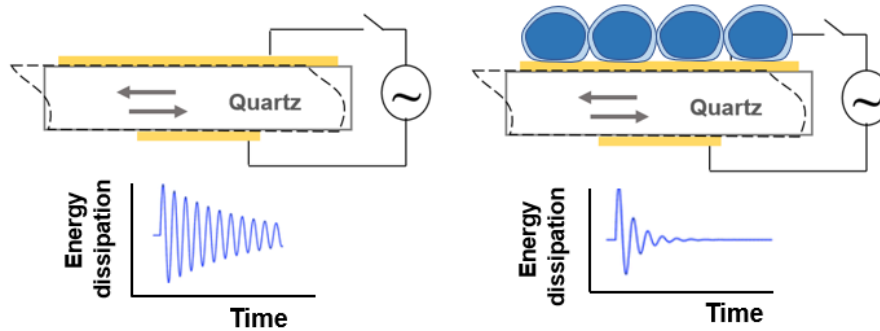229   energy dissipation response.

230

231   **Figure 1.** Schematic view of a QCM-D sensor excited by an AC voltage. Left panel: Bare Au-coated

232   sensor in liquid environment, the dampening of the oscillations takes place slowly. Right panel:

233   The presence of an adsorbed lipid vesicle layer (SVL) induces a faster damping of the oscillations

234   and thus a larger energy dissipation.

235   Commercial QCM-D instruments allow for monitoring changes in frequency and dissipation for

236   several overtones (n = 3, 5, 7,. . ., 13), Δf_n and ΔD_n, upon the presence of a nano/mesoscale layer.

237   The spectroscopic data at multiple frequencies with varying detection range enables assessing

238   the spatial homogeneity and rigidity of the adsorbed layer. For homogeneous thin and rigid

239   films, $\Delta D_n \sim 0$, Δf_n overtones overlap and a simple relationship between mass adsorbed and

240   change in frequency holds, the so-called Sauerbrey relation: $\Delta m = -C\Delta f / n$, with *C* being the

241   Sauerbrey constant which for a 5 MHz quartz crystal reads $C = d\rho_{quartz} / f_0 = 17.7 ng / cm^2$

242   (Sauerbrey, 1959). For thicker and softer films $\Delta D_n > 0$, overtones do not overlap and the

243   ensemble quartz-film-fluid can be represented by simple models combining elastic components

244   and viscous dashpots. These models enable to extract effective viscoelastic parameters of the

245   adsorbed film such as shear viscosity, thickness and shear storage modulus (Cho et al., 2007;

246   Voinova et al., 1999).

247   The capability of monitoring the viscoelastic properties during film formation is particularly

248   useful in the case of solid-SLB formation. QCM-D has been a valuable tool in deciphering the

249   kinetic pathways of SLB formation from precursor vesicles and how those depend on relevant

250 conditions such as solid surface adhesion strength, medium ionic strength, vesicle mechanics,

251 etc. (Cho et al., 2010; Jing et al., 2013; C. A. Keller & Kasemo, 1998; Pramanik et al., 2016; R P

252 Richter, 2006).

253 Figure 2 shows a typical QCM-D experiment where real-time monitoring of the adsorption of

254 zwitterionic DOPC vesicles onto SiO_2 and oxidized Au was carried out at 37 °C. The vesicles are

255 dispersed in TRIS-buffer (10 mM TRIS, 100 mM NaCl, pH 8) at a concentration of 0.1 mg/mL and

256 their hydrodynamic diameter d = 79 ± 20 nm. As initially discussed by Keller and Kasemo (C. A.

257 Keller & Kasemo, 1998), the adsorption kinetics is surface-specific. The mechanistic picture of Δf

258 and ΔD changes is governed by a delicate balance between the adhesive contribution to the free

259 energy from lipid-surface interactions and the opposing effect of bending and stretching the

260 membrane (Lipowsky & Seifert, 1991). DOPC vesicles adsorbing on SiO_2 follow a two-step

261 adsorption process consisting of i) adsorption of a critical number of vesicles and ii) fusion,

262 rupture and formation of an SLB. This is reflected in the Δf_n and ΔD_n signals depicted in the upper

263 panels of Figure 2. After a ~ 10 min baseline in buffer (Δf_n and ΔD_n = 0), DOPC vesicles added at

264 a very small flow rate adsorb onto the SiO_2-coated quartz sensor (Δf_n decreases and ΔD_n

265 increases) until a maximum number (minimum in Δf_n and maximum in ΔD_n). Adsorbed vesicles

266 then fuse and rupture as a consequence of the large adhesion strength of SiO_2, thus releasing

267 the entrapped aqueous buffer. As a consequence, Δf_n increases (mass loss) to a constant plateau

268 of Δf_n ~ −25 Hz and the ΔD_n signal decreases back to a very small value ($\Delta D_n < 0.5 \cdot 10^{-6}$). The final

269 Δf_n and ΔD_n values and the fact that overtones signals overlap is consistent with the formation

270 of a homogeneous rigid and thin DOPC SLB. The pathway of SLB formation is not unique and

271 depends strongly on the ionic conditions (head group charges of the constituent lipids, buffer

272 ionic strength presence of divalent cations, pH). Vesicles containing positively charged lipids like

273 DOTAP SUVs rupture individually on SiO_2 as a consequence of stronger vesicle-support

274 electrostatic interactions (R. Richter et al., 2003).

275 When DOPC vesicles adsorb onto an oxidized Au surface, a monotonic Δf_n decrease and ΔD_n

276 increase can be observed reaching constant non-zero plateau values with non-overlapping

277 overtones. Such time-dependent responses provide evidence that oxidized Au facilitates non-

278 ruptured vesicle adsorption towards the formation of acoustically non-rigid vesicle layers with

279 saturated coverage. As pointed out by Lind and Cárdenas (Lind & Cárdenas, 2016), it is worth

280 mentioning that local vesicle rupture events and formation of small bilayer patches cannot be

281 ruled out. As a matter of fact, QCM-D is very sensitive to hydrodynamic (wet) mass and the local,

282 partial formation of SLBs might be masked by the adsorption of vesicles on top or in between

283 the bilayer patches. In this case, complementary QCM-D and AFM measurements are

284   particularly useful to obtain a complete picture of the heterogeneous layers SLBs with co-

285   adsorbed vesicles formed. For example, the complementarity of AFM and QCM-D has proven

286   successful in experimentally confirming defect (protrusion)-driven nanoparticle interactions
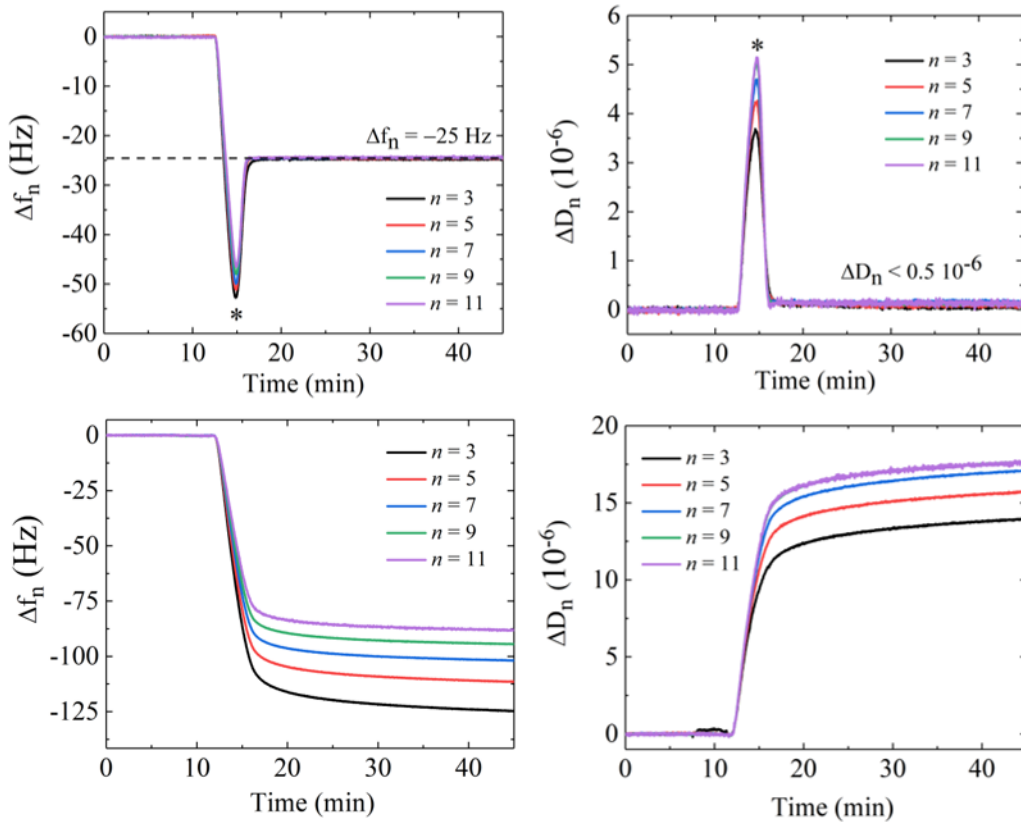
287   with SLBs (Van Lehn et al., 2014).

288

289   **Figure 2**. Time dependence of Δf_n and ΔD_n during a QCM-D experiment of DOPC vesicle adsorption

290   at 37°C onto SiO_2 (upper panels) and Au (lower panels).

291   Apart from kinetic information, QCM-D can be also useful to estimate the extent of vesicle

292   deformation upon adsorption following a model-free approach introduced by Tellechea *et al.*

293   (Tellechea et al., 2009). This method consists in plotting $-\Delta D/\Delta f$ ratio vs $-\Delta f$ for all overtones

294   during initial adsorption, which shows a linear decrease over a large range of frequency shifts.

295   Extrapolation of this linear decrease to a frequency-independent intercept with the $-\Delta f$ axis

296   (where overtones intersect) provides a value of the thickness of the adsorbed vesicle layer *h* or

297   Sauerbrey thickness: $h = -\Delta f\, C / \rho$, where C = 17.7 ng/cm^2 Hz and ρ = 1 g/cm^3 is the density of

298   the film. This approach assumes a complete surface coverage, where the presence of trapped

299   buffer has been diminished to occupy only the void spaces between densely packed vesicles (the

300    $-\Delta D/\Delta f$ ratio is close to zero and the $-\Delta f$ intercept values were the same on the extrapolation of

301   a linear regression) (Tellechea et al., 2009; Reviakine et al., 2012; Olsson et al., 2013). Figure 3

302 displays the extrapolated Sauerbrey thickness for DOPC SUVs adsorbed onto SiO_2 and Au

303 surfaces. The respective effective frequencies read h(SiO_2) = 30 ± 2 nm and h(Au) = 62± 5 nm. If

304 one compares these values with the original vesicle diameter in bulk measured by DLS (d =79 ±

305 20 nm), vesicles were deformed to a greater extent onto SiO_2 surfaces. A more exact approach

306 based on a hydrodynamic model was recently introduced by Cho and co-workers (Gillissen et

307 al., 2017) to estimate the deformation of small vesicles at low surface coverage. The model

308 enables to estimate adsorbed vesicle shape and bending energy by using hydrodynamic

309 spectroscopy (frequency shifts at several overtones). It treats vesicles as ellipsoids and relates

310 the so-called QCM-D force to the scaled viscous penetration depth δ/a with δ the viscous

311 penetration depth, and a the non-deformed vesicle radius, in order to probe the adsorbed

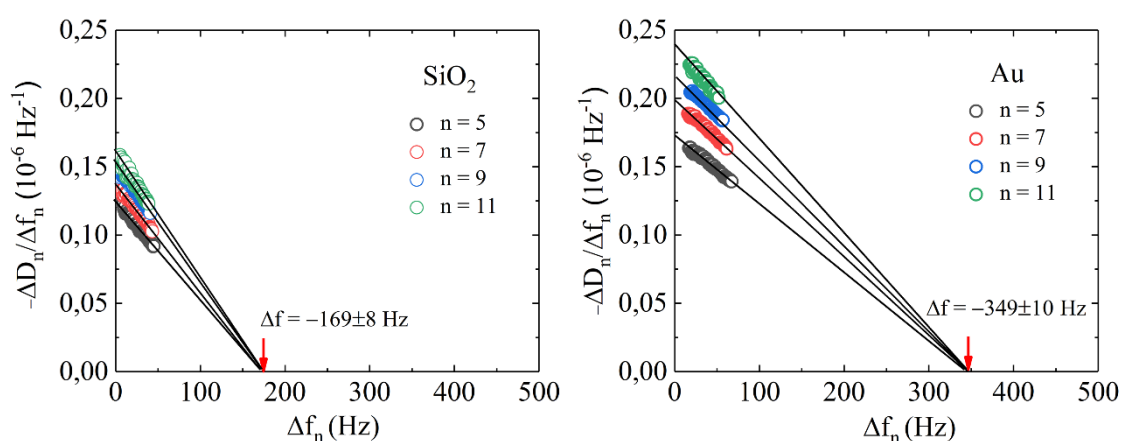312 particle aspect ratio. Further details on the model can be found in (Gillissen et al., 2017).

313

314 **Figure 3**. $\Delta D_n/-\Delta f_n$ ratio as a function of frequency at different overtones for DOPC vesicles

315 adsorbed onto SiO_2 and Au.

3.2. Atomic Force Microscopy (AFM)-based methodology

317 Classical structural techniques such as X-ray, NMR or electron microscopy rely on ensemble

318 averaging of molecular properties. Yet, by these means, the underlying molecular dynamics can

319 be hidden, since the signal comes from the average of many unsynchronized molecules in the

320 bulk. The picture changes when using single-molecule techniques. The measured signal of one -

321 or a few- molecules reflects the stochasticity of thermally induced processes when randomly

322 crossing free-energy barriers. Single-molecule optical microscopy techniques are particularly

323 well suited for the study of the dynamics of molecules. However, these latter methods rely on

324 the detection of fluorescent markers attached to proteins or lipids, which means that the

325 resolution is limited to ~200 nm due to diffraction of light and to a few tens of nm thanks to

326 super-resolution techniques. The atomic force microscopy (AFM) was since its invention in 1986

327 (Binnig et al., 1986) quickly positioned among the single-molecule, high-resolution structural

328   analysis techniques. It provides information concerning structure, function-related

329   conformational changes and supramolecular assemblies, crucial for a complete understanding

330   of biological processes. Nowadays, AFM is in its thirties and has become an invaluable tool for

331   studies at the micro- and nanoscale. As a stand-alone, high-resolution imaging technique and

332   force transducer, it is today an established methodology among the biophysical community. The

333   AFM uses a nanometer-sharp tip -resembling a record player needle- attached to a

334   (micro)cantilever to sense the sample surface while scanning it using piezoelectric elements. An

335   optical system is used to detect the cantilever deflection (or force), thanks to a laser diode beam

336   reflected on the back of the cantilever and detected by a photodiode. Changes in deflection due

337   to sample protrusions while the tip scans the sample are translated into electrical signals thanks

338   to a feedback mechanism. This is schematically represented in Figure 4.

339
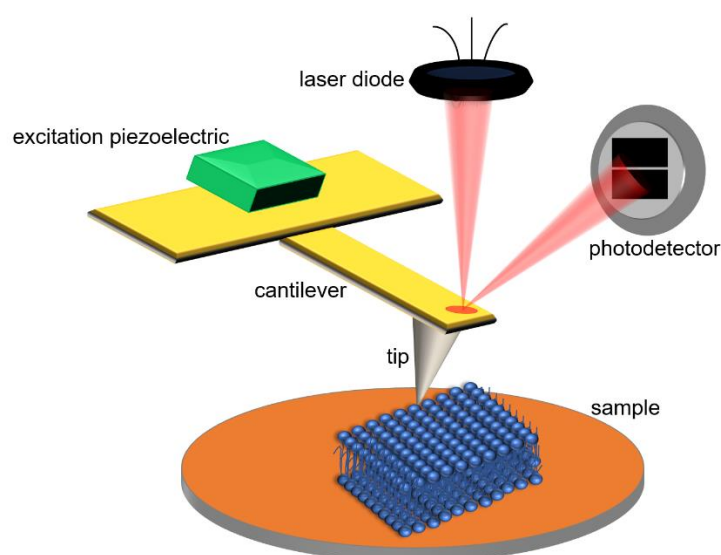
340   **Figure 4**. Schematic representation of an AFM instrument. The deflection of the cantilever in the

341   normal direction is monitored by a photodetector which collects the reflection of a laser beam

342   focused at the back of the AFM cantilever. In the tapping mode, thanks to a piezoactuator, the

343   AFM cantilever is excited near its resonance frequency.

344   One of the main strengths of AFM relies on the possibility of working in a controlled environment

345   (medium composition and temperature) and with great spatial resolution. AFM-imaging mode

346   provides submolecular resolution on a large variety of biological samples: from single molecules,

347   that is, DNA or proteins, to supramolecular assemblies such as SLBs, or even entire cells (Giles

348   et al., 1993)(Dufrêne et al., 2017; Parot et al., 2007). Therefore, AFM has become a well-

349   established technique for imaging the topography of lipid membranes that show homogeneous

350   or phase-separated morphology, permitting then to increase the bilayer complexity, from

351 bilayers of one component to multicomponent ones (El Kirat et al., 2010; B. Gumí-Audenis et al.,
352 2016a; Morandat et al., 2013; L Redondo-Morata et al., 2014).

353 For the study of biological samples, it is common to use AFM-imaging dynamic modes that have
354 an intermittent tip-sample contact. Among them, the most often used is oscillation or tapping
355 mode, in which the AFM cantilever is excited near its resonance frequency. The resulting
356 oscillating tip is intermittently contacting -tapping- the surface, giving rise to a damped
357 oscillation amplitude. Additionally, the resonance frequency is also shifted due to the probe-
358 surface interaction. The topography of the surface is reconstructed by monitoring the amplitude
359 of the oscillating cantilever, which is kept constant by adjusting the z-piezo position through a
360 feedback loop. While scanning in the X-Y direction, the amplitude of the cantilever oscillation is
361 kept constant thanks to a feedback control. However, biomolecules are dynamic in essence;
362 hence, to understand how biomolecules work it was only natural to think about increasing the
363 temporal resolution of conventional AFMs. The first time that the concept of High-Speed (HS)
364 AFM was mentioned -to our knowledge- was in 1991 by Barrett and Quate (Barrett, 1991), who
365 did a fairly attempt with the technology at that time. Other research groups, as Paul Hansma's,
366 would challenge the practical speed limitations. It was only in 2010 when the laboratory leaded
367 by Toshio Ando in Kanazawa University (Japan), filmed individual myosin molecules walking on
368 an actin filament (T Ando et al., 2008), operating their AFM instrument at a speed about 1000
369 times faster than the conventional instruments of that time. Besides the visual impact and
370 scientific insight of those movies, these experiments illustrated that HS-AFM could obtain
371 concomitantly structural and dynamic data, providing insights inaccessible by any other method
372 (Toshio Ando, 2017; Chiaruttini et al., 2015; Kodera et al., 2010; Mierzwa et al., 2017). The basic
373 principles, advantages and limitations of the most common AFM bioimaging mode are nicely
374 detailed in a recent review from Dufrêne *et al*. (Dufrêne et al., 2017).

375 Following the capability of the AFM for mechanical manipulation, to sense and apply small forces
376 accurately (pN-nN range), it rapidly developed into an excellent technique to study interactions
377 -inter and intramolecular forces- at the molecular level, the so-called AFM-based force
378 spectroscopy (AFM-FS). The manipulation of single molecules (single molecule force
379 spectroscopy) has led to fascinating new insights in the mechanics of proteins, polysaccharides,
380 synthetic polymers, and DNA at the molecular level (Florin et al., 1994)(Lee et al.,
381 1994)(Radmacher, 1997)(Noy et al., 1997)(Clausen-Schaumann et al., 2000)(Rief et al.,
382 1997)(Hugel & Seitz, 2001)(P E Marszalek et al., 1999; Piotr E Marszalek et al., 2001)(Giannotti
383 & Vancso, 2007).

384   In the case of lipid bilayers, AFM offers the unique opportunity to probe local physical and

385   mechanical properties, determining the interaction forces with nanoscale lateral resolution,

386   thereby providing new insights into membrane molecular mechanisms. For the nanomechanical

387   characterization with AFM, an SLB is generally first imaged and then a series of force-distance

388   curves is recorded over the same area. In each force-distance curve, the AFM tip away from the

389   surface is approached and retracted at constant velocity while the cantilever deflection is

390   recorded as a function of the Z piezo position. Each portion of the force-distance curve provides

391   information about the physical and mechanical properties of the bilayer, schematized in Figure

392   5. Upon mechanical contact during approach, the cantilever deflection increases and the SLB is

393   elastically compressed by the AFM probe until the tip suddenly breaks through the SLB, jumping

394   into a contact with the substrate (Figure 5, b). The first part of the curve, corresponding to small

395   elastic deformation upon compression, can be used to estimate elastic descriptors of the

396   membrane, like the Young modulus (E), the area compression-expansion modulus (K_A) and

397   bending modulus (k_C) (Dufrêne & Lee, 2000; Picas et al., 2012; L Redondo-Morata et al., 2016).

398   When performing very small elastic deformations (far from the bilayer rupture) it is also often

399   used for this calculation the retraction part of the curve. To estimate the elasticity of the lipid

400   film, the most common model used is the Hertz model, where the surface is approximate to an

401   infinitely half-space of an isotropic elastic solid and the indenter as non-deformable. The

402   parameter describing the sample is the Poisson's ratio (v), which depends on the nature of the

403   material. For soft biological samples, the Poisson's ratio is generally set to 0.5 (as for

404   incompressible materials). The geometry of the indenter determines the contact area. The

405   original Hertz model considers the shallow contact between two spherical bodies, but several

406   extensions were made for different indenter geometries (D. C. Lin et al., 2007). Again, when

407   performing experiments with small deformations far from the onset of the lipid bilayer rupture,

408   the hysteresis found between the approach and the retract curves is considered as dissipation

409   work and can be used to obtain intrinsic viscoelastic parameters of the viscoelastic material, by

410   the adaptation of common viscoelastic models as power-law rheology or the Kelvin-Voigt model

411   (Garcia et al., 2020).

412   Moreover, different types of short-range interactions can be measured -DLVO, hydration or

413   steric forces-, for further information review here (Lorena Redondo-Morata et al., 2012).
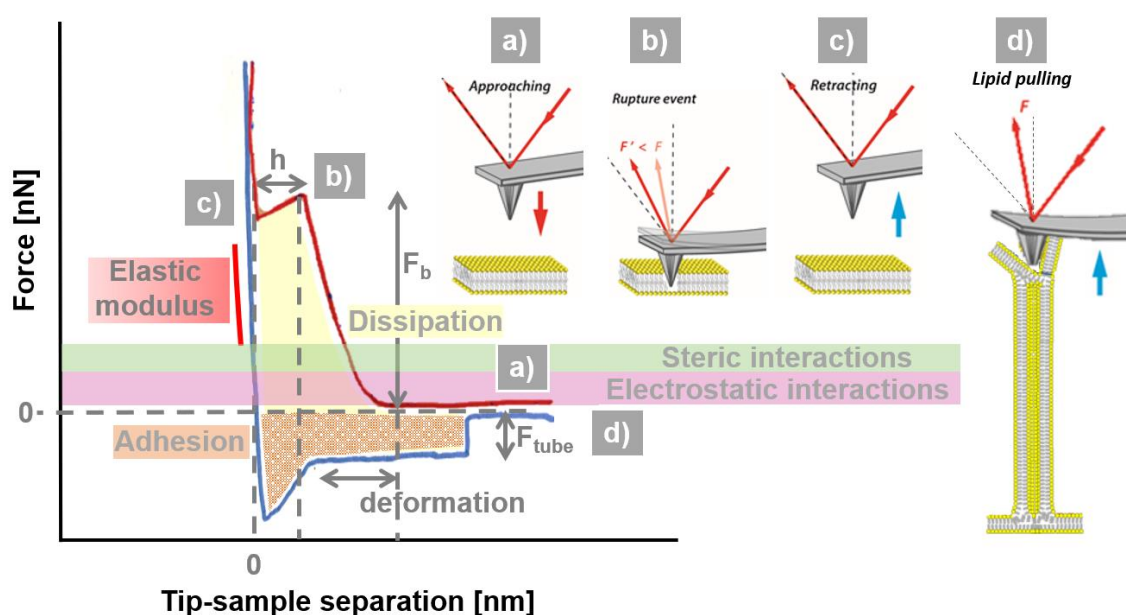
_____

414

Figure 5. Schematic representation of a representative force curve typically plot in vertical force vs. tip-sample separation. The red curve represents the tip approaching (a). Right after the contact area, short-range tip-sample interactions from different nature appear, predominantly electrostatic (highlighted in pink) and steric (highlighted in green) interactions. When keeping the tip velocity constant, elastic deformation of the membrane is followed by a sudden jump (b) which is interpreted as the breakthrough force (F_b) or the maximum force the bilayer is able to withstand before breaking. F_b has been extensively used as a hallmark of the bilayer stability, some of these related works are reviewed in this chapter. The AFM tip reaching the hard substrate underneath is represented as a vertical in the force-separation curve. From the distance in the curve between the breakthrough force and the substrate it can be estimated the minimal bilayer thickness (h) (fully compressed). Afterwards, tip retracts at constant velocity (c). Elastic modulus is usually estimated from the slope of the curve which displays membrane deformation. It is often observed a hysteresis between the approach and retract curves (yellow area) which is related to dissipation work and therefore to the viscoelasticity of the material. During retraction, negative force values are used to estimate the adhesion work between the sample and the AFM tip. Sometimes, a force plateau when retracting the AFM tip away from the SLB can be observed. It characterizes a tube pulling process (c'), defined by the tube growing force (F_{tube}) until eventually the AFM tip completely detaches.

The penetration of the AFM tip through the bilayer appears as a discontinuity in the approaching force-separation curve (Figure 5, b). The vertical force at which this discontinuity happens corresponds to the maximum force the bilayer is able to stand before breaking and is defined as the breakthrough force (F_b) or yield threshold force, first observed in the end of the 90's by

437   Dufrêne et al. (Dufrene et al., 1997, 1998)(Dufrêne & Lee, 2000; S Garcia-Manyes & Sanz, 2010;

438   B. Gumí-Audenis et al., 2016a; L. Redondo-Morata et al., 2012; Schneider et al., 2000). F_b is

439   generally of several nanonewtons (nN) and it is considered as a direct measurement of the

440   lateral interactions within the lipid bilayer, at a specified loading rate. From the step in the

441   separation before and after the breakthrough, the SLB thickness at different compression forces

442   (and at zero force) can be extracted.

443   The mechanical rupture of lipid bilayers is of thermal fluctuation nature, whose destructive

444   action is facilitated and directed by the application of the external force. The penetration of the

445   AFM tip through the SLB has been modeled and conceived as a two-state process with an

446   associated energy barrier (Butt & Franz, 2002; Franz et al., 2002; Simona Loi et al., 2002).

447   Specifically, two models describe the activation process. The first is the continuum nucleation

448   model, which considers the bilayer as a molecular thin homogeneous film -a two-dimensional

449   fluid layer- between the solid substrate and the solid surface of the AFM tip. The second model

450   ponders the molecular nature of the lipid bilayer and proposes that each molecule in the SLB

451   has specific binding sites corresponding to energetically favorable positions. These sites are

452   energetically equivalent, and as the SLB is pressed by the AFM tip, the energy of the molecules

453   significantly increases, leading them to jump apart and create a hole under the tip. After a critical

454   number of molecules have jumped out of the contact area, the tip indents the SLB due to the

455   high pressure of the remaining molecules, breaking the bilayer. Determining the energy barriers,

456   represented by the Arrhenius law, governing the lipid membranes rupture process contributes

457   to the understanding of the extent of the lateral interactions in the bilayer, and this is generally

458   achieved by following the variation of the F_b with the loading rate (r) by varying the tip-sample

459   approaching velocity (v) in what is called the dynamic force spectroscopy (DFS). Out of

460   equilibrium, the F_b increases linearly with the logarithm of r (and of v as well) (Butt & Franz,

461   2002; S Loi et al., 2002). The loading rate dependence with the thermomechanically activated

462   nature of the bilayer rupture kinetics leads to the evaluation of the activation energy of the

463   bilayer failure in the absence of an external force (ΔE_0). The activation energy ΔE for the

464   formation of a hole in the bilayer that is large enough to initiate rupture and lead the tip

465   breakthrough can then be calculated following the expression proposed by Butt et al.:

$$\Delta E(F_b) = -k_B \cdot T \cdot ln\left[\left(\frac{0.693 \cdot k_S}{A}\right) \cdot \frac{dv}{dF_b}\right] \qquad \text{(Eq. 1)}$$

466   where k_B is the Boltzmann factor, T is the absolute temperature, k_s is the cantilever spring

467   constant, A is the frequency at which the AFM tip attempts to penetrate the bilayer, generally

468   approximated to the resonance frequency of the cantilever, v is the tip velocity, and F_b the

469   breakthrough force.

470   When retracting the AFM tip away from the SLB, it sometimes remains connected to the bilayer

471   through a lipid tube (Figure 5, d). While the tip moves further away, the membrane tube grows

472   longer until it breaks at a certain distance, and the cantilever returns to the equilibrium position.

473   This tube pulling process occurs at constant force, the tube growing force (F_{tube}) (Armond et al.,

474   2011; Berta Gumí-Audenis et al., 2018; Maeda et al., 2002; Ralf P Richter & Brisson, 2003), and

475   it is observed as a force plateau in the retract part of the force-separation curve (Figure 5), at

476   several tens of pN from which F_{tube} and the tube growing distance (d) can be recorded. Pulling

477   lipid tubes with an AFM tip out of SLBs is a simplified but analogous situation to some biological

478   processes involving mechanical and conformational adjustments -bending, vesiculation,

479   tubulation-like formation of membrane tethers, endocytic vesicles, etc. (Schmidtke & Diamond,

480   2000; Shao et al., 1998; Sheetz, 2001; van Meer et al., 2008). Separation of a membrane segment

481   from the cytoskeleton as well as strong membrane bending are both involved, for which the

482   membrane chemical composition and physicochemical properties are key players. Pulling

483   tethers from cells with an AFM probe is a widely explored approach to evaluate the membrane

484   mechanics on entire cells (Brochard-Wyart et al., 2006; Marcus & Hochmuth, 2002; Nawaz et

485   al., 2015; Sun et al., 2005). Recently, it has also been established as a method to locally probe

486   SLB mechanics and the contribution of the underlying substrate to the measured properties on

487   SLBs (Berta Gumí-Audenis et al., 2018).

488   When pulling tethers from cells, the F_{tube} depends on the membrane properties like bending

489   stiffness (k_c) and in-plane membrane tension (σ), and also on the adhesion between the

490   membrane and the cytoskeleton (Sheetz, 2001). In regions where the membrane has separated

491   from the cytoskeleton -bleb or free membrane-, as there is no direct interaction with the

492   cytoskeleton, F_{tube} strictly relies on k_c and σ (Dai & Sheetz, 1999). However, the cytoskeleton

493   adhesion and σ are difficult terms to separate, and therefore the concept of apparent membrane

494   tension, σ_{app}, has been proposed to include the adhesion energy parameter γ (Sheetz, 2001),

495    $\sigma_{app} = \sigma + \gamma$. When the lipid tube grows under thermodynamic equilibrium, at the limit of zero

496   velocity (static thermodynamic analysis), the following mathematical expression relates the

497   membrane parameters mentioned above with the F_{tube} (Armond et al., 2011; Canham, 1970;

498   Daillant et al., 2005; E Evans & Yeung, 1994; Berta Gumí-Audenis et al., 2018; Hochmuth et al.,

499   1996; Marcus & Hochmuth, 2002; Roux, 2013): $\sigma_{app} = \frac{F_{tube}^2}{8k_c\pi^2}$.

500 The plus of this approach, AFM-based pulling lipid tubes from SLBs, is that it combines the

501 advantage of the AFM local probing with nanoscale lateral and force resolution, with the

502 simplicity of the SLB model preparation. Besides, the local nanomechanical properties of SLBs

503 can be explored through the combination of the tubing force spectroscopy approach and the F_b

504 analysis exposed before, within the same experimental procedure (Berta Gumí-Audenis et al.,

505 2018).

506 Although it will not be extensively discussed here, we find important to mention that the

507 constant force approach can also be used to evaluate the membrane rupture kinetics in SLBs

508 and supported lipid multibilayers (SLMs). The AFM tip is approached at constant velocity, and

509 then compresses the membrane at a constant force (force clamp, FC). Through measuring the

510 time it takes to penetrate the bilayer -time to breakthrough (t_b)- distribution at different

511 compression forces, the AFM-FC mode allows to estimate the rate of bilayer failure and calculate

512 the location of the energy barrier maximum -distance to the transition state- along the reaction

513 coordinate (Δx) and the activation energy (E_0) that characterize the energy barrier (L Redondo-

514 Morata et al., 2012a; Relat-Goberna et al., 2017). Both E_0 as well as Δx were found to be higher

515 for SLBs than for supported lipid multibilayers, endorsing previous suspicion that the mechanical

516 properties of lipid bilayers obtained from nano-indentation are strongly influenced by the

517 underlying hard substrate.

4. Phase behavior and nanomechanics. From one component membranes to higher complexity

4.1. One-component membranes

4.1.1. The gel and the fluid phase

522 To start with the simplest system and increase the complexity in this revision -which does not

523 intend to be exhaustive- consider a one-component phospholipid bilayer, which is thermalized

524 at a temperature far from its T_m, the temperature of the main phase transition, at which a

525 disordering of the hydrophobic tails happens followed by a sudden increase of the lateral

526 mobility. We are then able to distinct two different main phases, gel-like or solid ordered phase

527 (s_o) below T_m, and fluid-like phase or liquid disordered (l_d) above T_m.

528 A mechanical descriptor of lipid bilayers that shows significant differences between both phases

529 is the bending modulus k_c. At $T < T_m$, k_c is an order of magnitude larger than at $T > T_m$, rendering

530 lipid vesicles quite stiff, while softer and more deformable above T_m. In the case of SVLs, where

531 probing deformation is not straightforward, QCM-D has proved to be a useful tool to estimate

532 the extent of vesicle deformation upon adsorption onto surfaces. Reviakine and co-workers

533   (Reviakine et al., 2012) reported deformation measurements of small DMPC vesicles on TiO_2

534   above and below T_m, and experimentally found out that adsorbed vesicle deformation correlates

535   with the bilayer bending modulus. Liposomes in the fluid phase bear a smaller bending modulus

536   and deform to a greater extent.

537   When imaged with the AFM, the SLBs show typically 4-6 nm of height. The measured height is

538   also influenced by both the elasticity of each bilayer and the particular AFM methodology, *i.e.*

539   acoustic-modulation "tapping" mode, contact mode, etc, where the representation of the

540   interface of the lipid bilayer changes. In terms of its mechanical properties, whether we are

541   measuring the elastic deformation or the yield threshold force, a one-component SLB yields a

542   monomodal distribution. While the distribution of deformations or breakthrough forces of the

543   bilayer, being a stochastic process, have been often approached to Gaussian distributions, other

544   distributions based on different theoretical frameworks can also be found in the literature, like

545   the models proposed by Franz *et al*. (Butt & Franz, 2002) for the two-state activation process of

546   the bilayer rupture, mentioned in section 3.2.

547   In the first place, it could be said that, in a general way, the bilayer thickness depends on the

548   nature of the lipids -solid-like bilayers are usually higher than liquid-like counterparts of similar

549   number of carbons in the hydrocarbon chains. In an s_o phase, the hydrocarbon chains are

550   stretched, so the apparent height is greater, and this is observed when imaging SLBs by AFM.

551   Consequently, stretched acyl chains lead to stronger van der Waals interactions between

552   neighboring molecules, which translates into a shorter intermolecular distance between

553   phospholipids, and a greater mechanical resilience, both elastically and upon AFM tip

554   penetration.

555   For example, let's briefly consider the elastic deformation of DOPC and DPPC, as models of l_d

556   and s_o SLBs, respectively. The slope of the curve in the contact zone (elastic regime), as we have

557   commented in section 3.2, is related to the elastic modulus of the material. At room

558   temperature, the slope for the DOPC SLB, which is in the fluid phase, is lower than that for the

559   solid DPPC SLB. This indicates that DPPC bears a larger Young modulus than DOPC and thus the

560   membranes in the s_o phase are therefore stiffer than in the l_d phase. Both slopes are smaller

561   than the one that can be measured on the bare substrate (often assumed as an infinitely stiff

562   material, such as mica).

563   Besides the evidenced difference in elasticity for the fluid and gel-like membranes, l_d SLBs show

564   in general lower F_b values than s_o SLBs. A good example are homologous series phospholipids;

565   while at room temperature DLPC ($T_m \sim -2$ °C) SLBs break at force values between 2 and 13 nN,

566 according to the ionic environment, DPPC (T_m ~ 41.5 °C) SLBs are pierced by the AFM probe, in

567 similar conditions, in the force range that goes from 7 to 30 nN (Lorena Redondo-Morata et al.,

568 2012). It is also noticeable that the F_b increase with the logarithm of the loading rate is lower for

569 the fluid than for the gel membranes (Lorena Redondo-Morata et al., 2012). This can be

570 expected, if we consider the Bell-Evans or assimilable model, the most likely breaking force

571 depends linearly on the logarithm of the loading rate r, $F(r) = \left(\frac{k_B T}{x}\right) \ln \frac{rx}{K_0 k_{BT}}$, where k_B is the

572 Boltzmann constant, x is the distance to the transition state and K_0 is the off-rate constant at 0

573 force (E Evans & Ritchie, 1997). In this case, x is directly related to the distance between

574 neighboring phospholipid molecules. This intermolecular distance, therefore x, is smaller in s_o

575 than in l_d.

576 Early work showed how AFM-FS is able to explore quantitatively the molecular determinants

577 that provide mechanical stability to the supported membrane (S Garcia-Manyes, Oncins, et al.,

578 2005a; Sergi Garcia-Manyes et al., 2010). By systematically and independently changing the

579 chemical composition of the lipid headgroup, the length of the hydrophobic tail, and the number

580 of chain unsaturations,{Citation} it was possible to describe the mechanical stability of each

581 bilayer as a direct signature of membrane lateral organization (S Garcia-Manyes et al., 2010).

582 The distribution of F_b values as a function of the length of the hydrophobic chain showed that

583 on average, increasing each hydrocarbon tail by 2 extra –CH_2– groups results in ~ 7 nN increase

584 of the F_b, equivalent to an enthalpy increase by roughly 2 kJ/mol (Berg et al., 2002). In the same

585 study, the mechanical properties of the linear DPPC were compared with its analogous branched

586 phospholipid, DPhPC, to investigate the effect of acyl chain branching. The distribution of F_b

587 showed a decrease from ~20 nN to ~12 nN, revealing an important contribution of the lateral -

588 CH_3 groups on the molecular packing of the bilayer. This observation can be rationalized in terms

589 of the larger area per lipid for the branched DPhPC (76.8 Å^2) compared to that for the linear

590 DPPC (62.0 Å^2), as revealed by molecular dynamics simulations conducted in the fluid phase

591 (Shinoda et al., 2007). The nanomechanical effect of the –cis double bonds present in the acyl

592 chains was also investigated. The F_b values distributions for each particular bilayer showed an

593 inversely proportional trend between mechanical stability and number of unsaturations. It was

594 estimated that upon introduction of one additional unsaturation in each acyl chain, F_b values

595 decrease by ~5 nN. Interestingly, introducing an asymmetric unsaturation resulted in an even

596 further mechanical destabilization. The resulting molecular tilt reduces the effective packing

597 between molecules, giving rise to a lower T_m (Berg et al., 2002). The findings regarding the

598 mechanical implications of the headgroup chemistry were, however, far less straightforward

599 and highly unanticipated. Comparing phospholipids with the same hydrocarbon tails but

600   different headgroups, a huge range of forces required to indent the bilayer in the same

601   experimental conditions, spanning from ~3 nN (DPPA) all the way up to ~66 nN (DPPG).

602   Furthermore, the lateral packing differences observed between fluid and gel-like bilayers is also

603   reflected in the tube growing force, pulled as the AFM probe moves away from the SLBs, as this

604   approach has demonstrated to be sensible to the membrane chemical composition in one-

605   component SLBs (Maeda et al., 2002)(Berta Gumí-Audenis et al., 2018). Higher F_{tube} values for

606   DPPC with respect to DMPC have already been observed by Maeda *et al*. (Maeda et al., 2002)

607   and, as reported in Gumí-Audenis *et al*. (Berta Gumí-Audenis et al., 2018), F_{tube} is lower for l_d

608   mica-SLBs (in the range of 65–80 pN) than for s_o bilayers of the same headgroup (in the range of

609   90–110 pN) (Figure 6a). Additionally, while in the l_d state the F_{tube} slightly augments from PE to

610   PC (66 ± 15 pN for DOPE, 80 ± 25 pN for DOPC and 75 ± 13 pN for DOPG), it clearly increases

611   when changing the headgroup for s_o membranes from PE to PC and then PG (92 ± 20 pN for

612   DPPE, 104 ± 30 pN for DPPC and 112 ± 30 pN for DPPG). Hence, F_{tube} is generally higher for s_o

613   than for l_d and goes along with the lateral packing associated to different phospholipid

614   headgroups, in a way that is comparable to the trend observed on the F_b approach, as can be
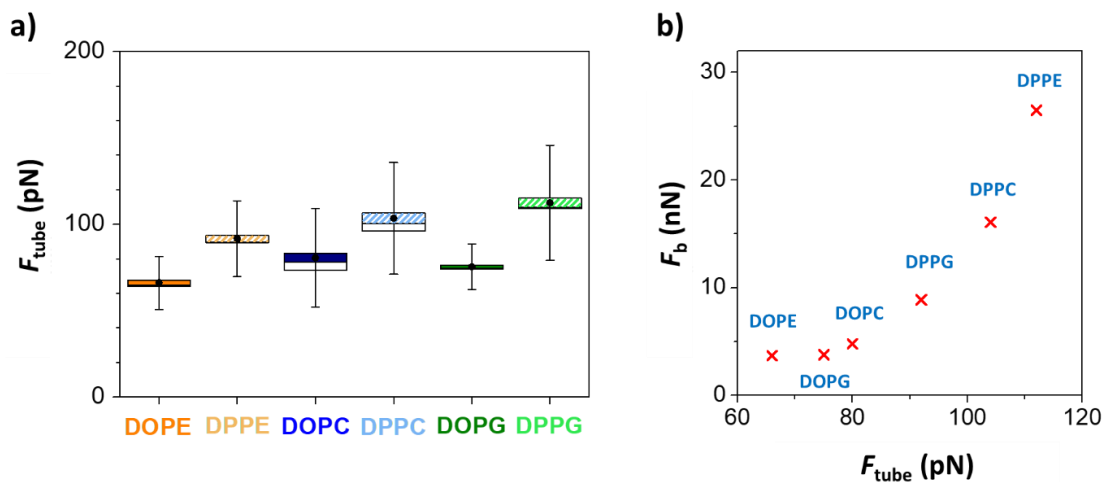
615   seen in Figure 6b.

616

617   **Figure 6**. AFM-pulling lipid tubes sensible to the membrane composition in one-component SLBs.

618   a) F_{tube} values for single component SLBs of different composition (DOPE, DPPE, DOPC, DPPC,

619   DOPG and DPPG). Boxchart for F_{tube} values show the mean (●), SE (box) and SD (bars). b)

620   Correlation between F_b and F_{tube} values for single component SLBs. The individual phospholipids

621   contain a constant tail length of 18 C with 1 unsaturation (DOPE, DOPG and DOPC) or 16 C and

622   fully saturated (DPPE, DPPC and DPPG), in fluid and gel state at room temperature (RT),

623   respectively. All the measurements were performed in 150 mM NaCl, 20 mM MgCl$_2$, 20 mM

624   HEPES (pH 7.4) buffer solution and at RT. Adapted from Ref. (Berta Gumí-Audenis et al., 2018)

625   with permission from the Royal Society of Chemistry.

626   Taken together, force spectroscopy experiments on SLBs are in qualitative agreement with the

627   literature that correlates the physicochemical properties of membranes with the chemical

628   composition of their phospholipid hydrophobic chains (Rawicz et al., 2000). Noteworthy,

629   thermodynamic quantities such as the melting temperature or the order parameter can be

630   translated into the realm of mechanical stability. The order parameter is usually calculated from

631   NMR-based measurements and provides information about the overall membrane order and

632   more particularly the conformations that the atoms within the lipid tails adopt (Piggot et al.,

633   2017).

634   ## 4.1.2. The thermal transition

635   ### *4.1.2.1. Main transition*

636   A useful application of QCM-D is the detection of thermotropic phase transitions within SLBs

637   and SVLs, with the asset that it is label-free, it does not require long temperature equilibration

638   times nor a large amount of sample. When temperature is varied in the absence of any

639   transition, Δf and ΔD typically show a regular, linear temperature dependence, as a reflection of

640   regular, temperature-dependent changes of the viscosity and density of the surrounding liquid

641   medium. When approaching the main phase transition temperature, both frequency and the

642   dissipation responses will differ from a regular temperature dependence, displaying anomalies

643   that reveal that structural changes are taking place (Losada-Pérez et al., 2014; Neupane et al.,

644   2018). Figure 7 displays changes in the frequency and its derivative of an SVL of DMPC of vesicles

645   of around 130 nm, with main transition temperature $T_m \sim 24$ °C in a rather narrow temperature

646   range. The shape of frequency shift curves and its respective temperature derivative are

647   reminiscent of the enthalpy jump and its heat capacity derivative typically obtained from

648   calorimetric measurements (Heimburg, 1998; Losada-Pérez et al., 2014). Dissipation typically

649   shows jumps and minima in the same temperature range. Therefore, extrema in the first-order

650   derivative of frequency and dissipation curves stand as a token of the layer thermotropic phase

651   transitions. Calorimetry is a state-of-the art technique for the detection of phase transitions

652   based on changes in thermal properties when lipids undergo the main (first-order) transition

653   (heat absorption or release), while QCM-D is based on changes in viscoelastic properties of the

654   adsorbed vesicles as a result of changes in bilayer thickness, rigidity and vesicle shape. Although

655   also detectable in SLBs, the size of the jumps in Δf and ΔD is several orders of magnitude smaller

656   than the size of the jumps observed for SVLs (Wargenau & Tufenkji, 2014; Hasan & Mechler,

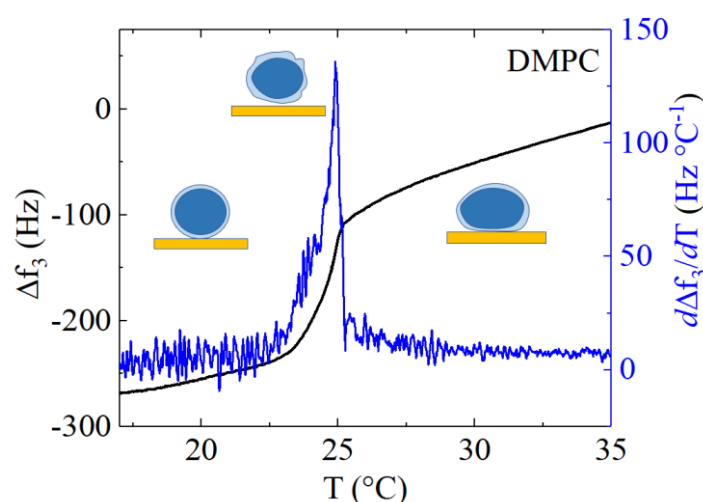657   2015).

658

Figure 7. Temperature dependence of the frequency shift dΔf_3/dT (black solid line) and its first-order derivative (blue solid line) of a DMPC SVL upon heating at 0.2 °C/min.

Reviakine and coworkers provided a comprehensive interpretation of the mechanisms by which QCM-D detects phase transitions in lipid membranes and the related relative contribution of thickness, stiffness and hydrodynamic channels to the Δf and ΔD fingerprints (Peschel et al., 2016). Upon heating, lipid bilayers in both SVLs and SLBs change from a thicker and stiffer s_o phase to a thinner and less stiff l_d one. Both stiffness and thickness changes in the lipid layer properties across the transition encompass changes in the Δf signal (decrease upon heating). In the case of the ΔD, the stiffness and the thickness contributions oppose each other since stiffer layers dissipate less. In the SLBs, this leads to an overtone dependence of the transition peak (Peschel et al., 2016). In thicker and softer SVLs, changes in the shape of the adsorbed vesicles might induce further hydrodynamic channels that contribute to ΔD. As a consequence, the size of the maximum in SVLs is several orders of magnitude larger than the one observed in SLBs.

The thermotropic phase behavior of pure SLBs has been widely related with the (nano)mechanical properties of the bilayer. Combining the previously exposed approaches, the AFM-FS sensitivity to the lipid phase of SLBs is evidenced, positioning it as an appropriate tool to determine the phase thermal transitions. Temperature controlled-AFM has been established as a suitable tool to analyze both the topographical and mechanical evolution of biologically relevant issues that are temperature dependent at the nanometer scale.

Seminal work of Leonenko *et al*. demonstrated the existence of several phase transitions in DPPC and DOPC mica-supported bilayers (Z. V. Leonenko et al., 2004). Data of both topographical imaging and force measurements provide invaluable insight into membrane behavior during phase transitions. For DPPC SLBs, F_b values decrease as temperature increases, and beyond the

682   main transition, DPPC shows similar force plots as the fluid-phase DOPC bilayers. This

683   dependence of the F_b on the phase state of the SLB below and above T_m has been further

684   reported for different lipids, like DMPC ($T_m \sim$ 24 °C) that changes F_b from 13-14 nN at 20 °C

685   below T_m to about 6 nN at or 40 °C DPPC ($T_m \sim$ 42 °C) that shows a switch of F_b from around 20-

686   25 nN at 27 °C to around 3-5 nN at 55 °C (S Garcia-Manyes, Guell, et al., 2005; L Redondo-Morata

687   et al., 2012b). When the DPPC SLB is maintained a temperature slightly above T_m, coexistence

688   of the gel and fluid phase occurs and a bimodal F_b distribution is obtained (Figure 8), as reported

689   in Gumí-Audenis *et al.* (B. Gumí-Audenis et al., 2016a). This is because the thermal transitions in

690   SLBs generally happen at temperatures slightly higher and in a broader range than in vesicle

691   suspensions as a consequence of the underlying substrate affecting lateral order and interleaflet

692   coupling (S Garcia-Manyes, Guell, et al., 2005; Z. V Leonenko et al., 2004; L Redondo-Morata et

693   al., 2012b; Seeger et al., 2010). In Garcia-Manyes *et al.* it was shown that the main phase

694   transition occurs in a range of temperatures of *ca*. 10-13 °C (S Garcia-Manyes, Oncins, et al.,

695   2005b).

696   There is an effect of temperature on the mechanical stability for the SLBs because the increase

697   of temperature directly affects the molecules fluctuations provoking an increment in the area

698   per molecule -lower packing density-, especially noticeable in the gel phase, with the

699   consequent decrease of the F_b values. At temperatures around the T_m of the lipid, and for a

700   temperature range of a few °C, a pronounced drop in F_b takes please, as the SLB gradually

701   transitions to the fluid phase, thereby softening. Several degrees over the T_m, the F_b values are

702   on the order of the ones typically observed for l_d SLBs at room temperature (Alessandrini & Facci,

703   2012; S Garcia-Manyes, Oncins, et al., 2005a; L Redondo-Morata et al., 2012b). This can be seen

704   in the example shown in Figure 8d, where the DPPC mica-SLB shows an F_b value around of 21

705   nN at 27 °C and slight decreases with temperature as the 42–45 °C range is reached. At higher

706   temperatures, the F_b remains approximately constant at *ca*. 3.5 nN. The F_b-temperature trend

707   displays a break around the T_m value of DPPC.
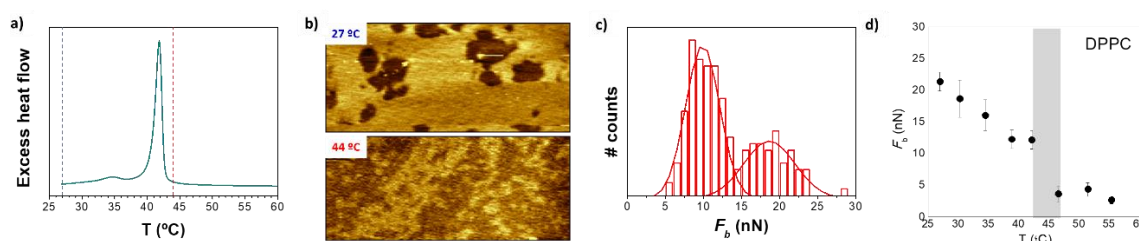

708

709   **Figure 8.** Phase transition of DPPC bilayers: a) DSC thermogram of DPPC vesicle suspension; b) 6

710   μm x 2.5 μm AFM images of DPPC silicon-SLB at 27 ºC and 44 ºC; c) F_b histogram at 44 ºC and

711 gaussian fits to the bimodal distribution. All experiments performed in 150 mM NaCl, 20 mM

712 MgCl$_2$, 20 mM HEPES (pH 7.4) buffer solution. Adapted from Ref. (B. Gumí-Audenis et al., 2016a).

713 d) Mean F_b value of DPPC mica-SLB as a function of temperature, in 10 mM HEPES, 20 mM MgCl$_2$

714 and 150 mM NaCl (pH 7.4). The shadowed vertical line marks the observed transition

715 temperature range. Adapted from Ref. (L Redondo-Morata et al., 2012b)

716 Additionally, Mouritsen and coworkers proposed that AFM topography at a varying temperature

717 could decouple the phase transition of the two different leaflets of the mica-supported bilayer

718 (D. Keller et al., 2005). The low temperature transition was proposed to be related to the melting

719 of the leaflet far from the substrate surface, and the second transition to the phase transition of

720 the leaflet in contact with the mica. Such decoupling would respond to the stronger interaction

721 between the lipid headgroups of the proximal monolayer and the mica support.

722 *4.1.2.2. Pretransition*

723 Some lipids present a pretransition before the main first-order transition which gives rise to an

724 intermediate order in the lipid bilayers referred to as ripple phase. Ripple phases are curved

725 structures with undulating surface topography. AFM imaging revealed the structure of the ripple

726 phase in hydrated conditions at the nanometer scale (Kaasgaard et al., 2003), and such particular

727 structure has been recently explored nanomechanically (Majewska et al., 2020). It can be found

728 when solid phase lipids experience an increase in temperature and go into the fluid phase, and

729 alternatively it occurs when the fluid phase is cooled down. The observation of this phase

730 transition process is characterized by a melting point temperature of the ripple phase to fluid

731 phase, nucleation point and growth directionality for the formation of the ripple phase. HS-AFM

732 coupled to a temperature-controlled system can report directly ripple to fluid phase transitions

733 (reversibly) in real time and at high resolution (Takahashi et al., 2016). Transition processes from

734 ripple phase to fluid phase and from ripple phase to metastable ripple phase to fluid phase,

735 could be reversibly, phenomenologically and quantitatively studied. In Takahashi *et al*., results

736 showed phase transition hysteresis in fast cooling and heating processes, while both melting

737 and condensation occurred at 24.15 °C in quasi-steady state situation. A second metastable

738 ripple phase with larger periodicity was formed at the ripple phase to fluid phase transition when

739 the buffer contained Ca^{2+}. Thermodynamically, a lipid system containing small domains does not

740 necessarily correspond to a phase coexistence regime, but they may constitute a one phase

741 regime with micro- or nanoscale heterogeneities[1] (Heimburg, 2000). Altogether, these findings

_____

[1] We will further visit this topic in Section 5).

742 may have relevance in more complex cellular systems where lipid nanodomains form and
743 dissociate reversibly.

4.2 Phase coexistence

745 Phase segregation and coexistence in lipid bilayers generally happens in the simplest models
746 when mixing a fluid and a gel-like phospholipids, and in the more complex mixtures, like those
747 containing phospholipids, sphingomyelins, ceramides, and cholesterol. At room temperature
748 the bilayers composed of a mixture of a gel and a fluid phospholipid generally segregate into
749 different domains, showing a continuous fluid phase enriched with l_d lipid and thicker dispersed
750 domains associated to a phase enriched in the s_o lipid. When the T_m of the gel-phase lipid is
751 overcome, the binary phospholipid system becomes homogeneous and fluid. Among the many
752 that can be found in the literature, we here mention some examples of these binary systems.

753 The capability of QCM-D to detect lateral phase coexistence and map phase diagrams for binary
754 lipid mixtures of saturated phospholipids will be provided for binary mixtures of homologous
755 phosphatidylcholines DMPC and DSPC, whose chemical structures differ in four methylene
756 groups. This system has been thoroughly investigated experimentally and theoretically in free
757 standing lipid systems (Ehrig et al., 2011; Fidorra et al., 2009; Mabrey & Sturtevant, 1976).
758 DMPC:DSPC mixing behavior is driven by the large hydrophobic mismatch between the two
759 components and departs from ideality as a consequence of the large difference in T_m of the pure
760 constituents.

761 Figure 9 (left panel) shows representative QCM-D signature of phase transitions we now revisit
762 taking place upon heating pure SVLs of pure DMPC and three DMPC:DSPC mixtures (Losada-
763 Pérez, Mertens, et al., 2015). The diameter of the precursor vesicles forming the SVLs was
764 around 130 nm. For pure DMPC, the main transition takes place in a rather narrow temperature
765 range around $T_m \sim 24$ °C. The first-order derivatives of Δf curves capture the typical behaviour
766 of two-component lipid mixtures displaying s_o and l_d phase coexistence. As very low DSPC
767 concentration (DSPC mole fraction = 0.1), the transition is shifted towards higher temperatures
768 and takes place in a broader temperature range indicating a loss of intermolecular cooperation
769 between DMPC molecules to undergo the main transition due to the presence of DSPC. For the
770 mixtures close to the equimolar concentration two small peaks can be observed indicating the
771 coexistence of two phases, s_o and l_d. The peaks are not simple additions of the peaks of the
772 individual constituents, the size of each peak scales with the concentration of each lipid in each
773 coexisting phase. For instance, the inset of Figure 9 displays the peaks of the mixture
774 DMPC:DSPC (40:60). The low-temperature peak corresponds to the DMPC-rich phase, while the

775   high-temperature peak to the DSPC-rich phase. As expected, the size of the latter is higher, since

776   the concentration of DSPC in the mixture is larger.

777   The analysis of the peaks using the tangent method (Ehrig et al., 2011) to determine the onset

778   and completion temperatures enables to map the phase diagram of this mixture. The solid lines

779   are added as a guide to the eye, delimiting the phase coexistence region, dark red (liquidus line),

780   light blue (solidus line) and follow experimental heat capacity values by Maubrey *et al.* (Mabrey

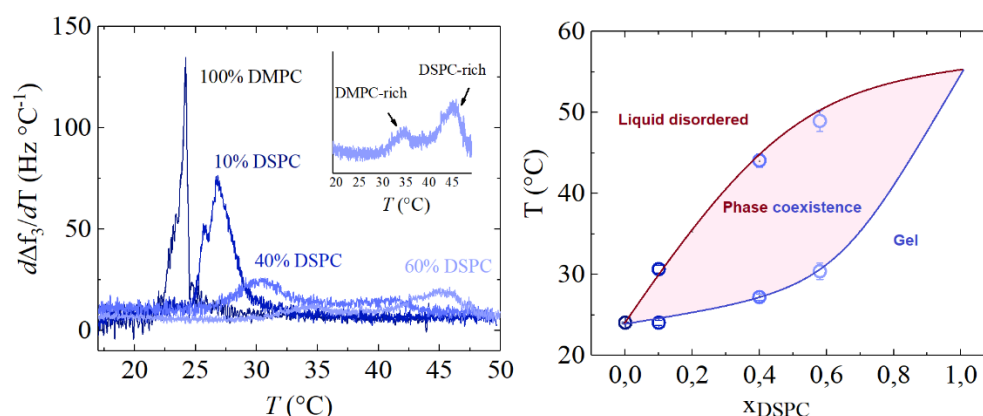781   & Sturtevant, 1976) obtained for multilamellar vesicles of the same concentration.

782

783   **Figure 9.** Left panel: temperature profiles of the first-order temperature derivative of the

784   frequency shifts for pure DMPC and DMPC:DPSC mixtures 10%, 40% and 60% mole fraction (in

785   percentage) of DSPC. Right panel: phase diagram obtained from extracting onset and completion

786   temperatures from the peaks (Losada-Pérez, Mertens, et al., 2015).

787   As discussed in the previous sections, the nanomechanical properties determined by AFM-FS on

788   SLBs are distinctive of the chemical structure and molecular organization of a bilayer at specific

789   environmental conditions. This allows for a direct correlation of the elastic modulus, F_b, or F_{tube}

790   values with the composition in phase-segregated membranes. In most cases, the AFM

791   topographical characterization easily identifies the segregation of an SLB in different domains,

792   due to their difference in thickness and compressibility. However, it is possible to reveal the

793   presence of different domains in an SLB on the basis of their different mechanical properties

794   even when the domains have a height difference which is too small to be detected by

795   conventional imaging.

796   Bernchou *et al.* studied, using combined fluorescence microscopy and AFM, the nucleation and

797   growth of domains in equimolar binary SLBs composed by DOPC and DPPC (Bernchou et al.,

798   2009), a mixture that shows coexistence of l_d and s_o domains at room temperature (Z. V.

799   Leonenko et al., 2004). These authors could observe that during cooling the shape of the

800   domains evolved from compact to a branched morphology, which they discussed as the domain

801   growth being controlled by the diffusion of DPPC from the liquid phase toward the solid domain

802   interface. In the late stages of the growth, the size and overall shape of the domains depend on

803   the position of the nucleation points relative to the surrounding nucleation point positions.

804   A mechanical contribution concerning the elastic deformation of the membrane before the

805   breakthrough point should be considered to fully comprehend the force-distance curve. A

806   method to study the elastic properties consists of quantitative nanomechanical mapping (Picas

807   et al., 2012). In (L Redondo-Morata et al., 2016), the equimolar binary lipid mixture DPPC:DOPC

808   was studied, where l_d and s_o coexisting domains in SLBs are large and directly visually discernable

809   by AFM imaging (Figure 10a) with clearly distinguishable heights (~0.8 nm height difference,

810   Figure 10b). Elastic modulus nano-mechanical mapping (Figure 10c) shows good agreement

811   with the E values in the literature, characterized mechanically by AFM (Picas et al., 2012; Rawicz

812   et al., 2000) and micropipette aspiration (Dieluweit et al., 2010). The mean E values are

813   26^{+58}_{-12} MPa for the l_d domain and 33^{+75}_{-15} MPa for the s_o domain, respectively (Figure 10d).

814

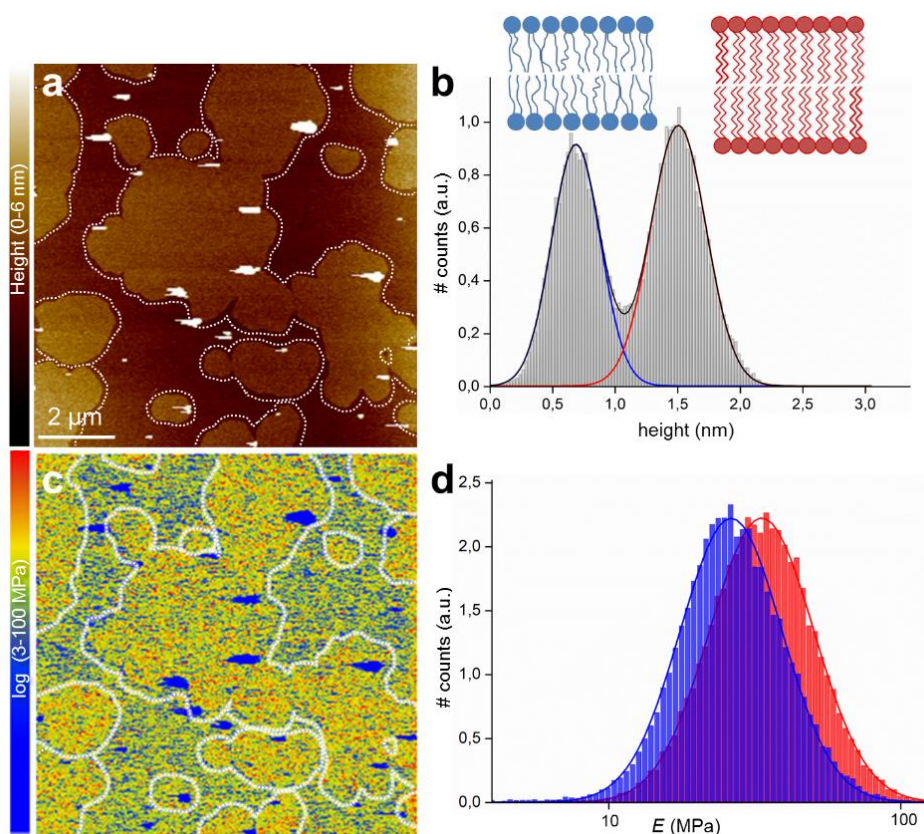815   **Figure 10.** PF-QNM AFM Topography and Elasticity mapping of DOPC:DPPC (1:1) SLBs. a)

816   Topography image (nm) and b) height histogram analysis of the topography (a). The dashed lines

817   in a) represent the domain edges defined by edge detection. The solid lines in b) are Gaussian fits

818   to the height distribution, indicating an average height difference between the DOPC l_d (blue line)

819   and DPPC s_o (red line) domains of 0.82 nm. c) The corresponding stiffness map (log scale, MPa)

820   and d) Young's modulus values histograms (log scale, MPa) of the regions outlined in the

821   topography (a) and stiffness (c) maps, corresponding to the DOPC (blue) and DPPC (red) domains.

822   The solid lines are Gaussian fits to the distributions peaking at 26^{+58}_{-12} Mpa (DOPC) and 33^{+75}_{-15} Mpa

823   (DPPC) (from reference (L Redondo-Morata et al., 2016) with permission).

824   Using the Young modulus for each domain of the DOPC:DPPC mixture together with the

825   experimental bilayer thickness (h), the thin shell theory can be used to calculate the area

826   compression-expansion modulus (K_A) and bending modulus (k_C) as (Rawicz et al., 2000):

827
$$K_A = \frac{Eh}{(1 - \nu^2)} \quad \text{and} \quad k_c = \frac{Eh^3}{24\,(1-\nu^2)}$$

828   When lipid domains separate in lipid mixtures, or when lipids surround membrane embedded

829   proteins there is, in general, a hydrophobic mismatch at the domain interfaces (Wallace et al.,

830   2006) or protein/bilayer interfaces (Mouritsen & Bloom, 1984), with an ensuing compression or

831   stretching of the hydrocarbon chains in the vicinity of the interface. This hydrocarbon tail

832   stretching or compression may influence the distribution of domain sizes and the kinetics of

833   domain separation, as well as membrane protein function. The compression/stretching of the

834   acyl chains of the s_o and l_d domains can be determined by minimizing the elastic energy of the

835   system, $G_s(x)$, expressed assuming volume conservation (Wallace et al., 2006) as

836
$$G_s = \frac{K_O A_O}{2h_O^2}(x - h_O)^2 + \frac{K_D A_D}{2h_D^2}(x - h_D)^2 \qquad (2)$$

837   where K_o and K_d are the stretch moduli for s_o and l_d, respectively. A_o and A_d are the lipid area

838   per molecule for s_o and l_d, respectively. A values are well-documented in literature (notably

839   through X-ray diffraction and Langmuir methods), being 0.72 nm^2 for l_d DOPC and 0.49 nm^2 for

840   s_o DPPC at room temperature (Nagle & Tristram-Nagle, 2000). h_o and h_d are the measured

841   bilayer thickness of s_o and l_d, respectively. The estimated G_s values for the DOPC l_d and the DPPC

842   s_o domains are 0.27 k_BT. Hence, the experimental determination of E allows to estimate the

843   stretch modulus and the bending stiffness of the lipid membrane, as well as the energetic cost

844   of the lipid domains to accommodate to different thickness.

845   For the SLB system composed of a POPE:POPG mixture (Picas et al., 2009), AFM images revealed

846   the existence of two separated phases, the higher showing a region with protruding

847   subdomains. AFM-FS was then used to clarify the nature of each phase. The values of F_b,

848   adhesion force and height extracted from the force curves were assigned to the corresponding

849   s_o (the mechanically stable domains) and l_d phase (the mechanically labile phase). In Crespo-

850   Villanueva *et al.*, while the SLB composed of equimolar DSPC:DOPC was shown to phase

851   segregate, clearly demonstrated in the AFM topographical images and the correlative F_b maps

852   and bimodal distributions around ~40 nN and ~5 nN, the equimolar mixture of the two l_d lipids

853   DOPC:DOPS led to a homogeneous topography and narrow F_b distribution around 3.5 nN

854   (Crespo-Villanueva et al., 2018). In Domenech *et al.*, they studied ternary mixtures of

855   POPC:POPE:CL, a minimum system that mimics the mitochondrial inner membrane (Domenech

856   et al., 2007). They could observe laterally segregated domains whose height decreased with

857   increasing temperatures.

858   Pulling lipid tubes with the AFM probe also allows to characterize phase segregated bilayers and

859   laterally resolve the different domains in multicomponent SLBs (Berta Gumí-Audenis et al.,

860   2018). This is exemplified in Figure 11, a bilayer composed of the l_d lipid DOPE and the s_o lipid

861   DPPG in ratio DOPE:DPPG 25:75, that at room temperature forms SLB patches with coexisting

862   domains: gel-phase rich in DPPG, dispersed in fluid-phase rich in DOPE. When indented by the

863   AFM tip at a constant velocity of 1 μm s^{-1}, a bimodal F_b distribution is obtained, with

864   differentiated mean F_b values associated with the fluid (~5 nN) and gel (~12 nN) domains.

865   Analyzing the retract force-separation curves that showed the tube pulling event allowed to

866   represent the F_{tube} distribution and map, where the lower force values (red pixels) are

867   distributed in the peripheral part of the SLB patch and higher forces (yellow pixels) in the center,

868   and the F_{tube} distribution is resolved when sorting according to the corresponding F_b, giving a

869   mean value of 75 ± 20 pN for the DOPE-rich phase, and 112 ± 25 pN for the DPPG-rich phase.

870   The fact that F_b and F_{tube} for the domains slightly differ from the values for pure DOPE and DPPG

871   SLBs allows to infer partial miscibility among them.
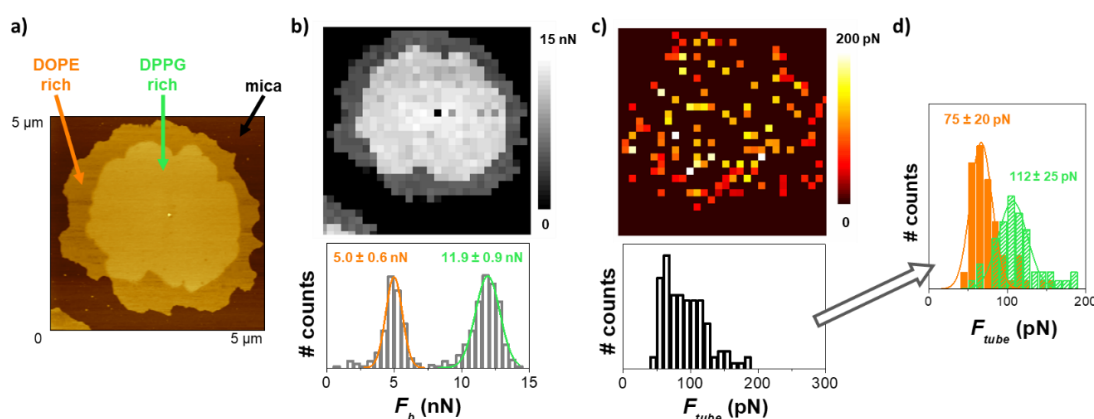

872

873   **Figure 11.** DOPE:DPPG (25:75). a) AC-mode AFM topographical image; b) F_b map and distribution;

874   c) F_{tube} map and distribution; d) F_{tube} distributions resolved by filtering according to the F_b

875   distribution. Reproduced from Ref. (Berta Gumí-Audenis et al., 2018) with permission from the

876   Royal Society of Chemistry.

877   Higher complexity models, like the ternary lipid mixtures containing an unsaturated

878   phosphatidylcholine (PC), a saturated PC or sphingomyelin (SM), and Cholesterol (Chol) have

879   been probably the most studied due to the physiological abundance of these lipids. Depending

880   on the ratio of the components, these mixtures have shown to exhibit two coexisting fluid

881   phases: an l_o phase that is enriched in Chol and SM or saturated PC, and an l_d phase that is

882   predominantly composed of unsaturated PC (Johnston, 2007), and the possibility of a coexisting

883   s_o phase. The group of Schwille has extensively analyzed the domain organization in

884   DOPC/SM/Chol model membranes by means of AFM in combination with fluorescence

885   correlation spectroscopy (FSC) (S Chiantia, Kahya, et al., 2006; S Chiantia, Ries, et al., 2006;

886   Salvatore Chiantia et al., 2007, 2008) and by performing AFM-FS experiments on the different

887   phases they have shown that the average force needed to pierce the l_o phase of the

888   DOPC/SM/Chol bilayer is about 4 nN higher than the one needed to pierce the l_d phase. In a

889   parallel study, Zou and coworkers explored the influence of different cholesterol contents on

890   the morphology and (nano)mechanical stability of phase-segregated DOPC/SM/Chol lipid

891   bilayers by means of AFM imaging and force mapping (R M A Sullan et al., 2010). They observed

892   consistently higher F_b values in the SM/Chol-enriched l_o domains than in the DOPC-enriched l_d

893   phase, and that the (nano)mechanical stability of both coexisting phases counterintuitively

894   decreased with increasing Chol content. By following the dependence of the F_b value with the

895   loading rate in both phases, they calculated the activation energies (ΔE_0) of bilayer rupture at

896   zero applied force. ΔE_0 values obtained were in the range 75-125 kJ/mol for all tested Chol

897   contents and did not show a dependence on the different lipid phases.

898   Besides sphingolipids, ceramides (Cer) have also gained attention in physicochemical studies by

899   means of AFM, since they are known to be predominant in physiologically relevant nanodomains

900   -which have been controversially called for many years lipid rafts (Goñi, 2019a). Longo and

901   coworkers observed that DLPC/GalCer/Chol ternary mixtures only display l_d/s_o coexistence and

902   no l_o phase even at high Chol content (Blanchette et al., 2006). By measuring the area/perimeter

903   ratios of the segregated domains, the authors concluded that Chol was able to decrease the line

904   tension between the two phases. In another study (W.-C. Lin et al., 2007), they could also

905   observe a phase coexistence attributed to l_d/l_o phases with POPC and DOPC at 10 mol% Chol, an

906   indication that fatty acyl chain unsaturation, cholesterol ratio and lipid hydrophobic mismatch

907   in the organization of multi-component lipid systems.

908   Ceramide incorporation on coexisting fluid phase and ordered domains in phase-separated

909   binary and ternary lipid mixtures was shown to affect the lipid spatial organization in domains,

910   with the appearance of a Cer-enriched gel-like phase and the displacement of cholesterol from

911   rafts (S Chiantia, Kahya, et al., 2006; Salvatore Chiantia et al., 2007; Ira et al., 2009). In order to

912   directly probe and quantify the (nano)mechanical stability and rigidity of the Cer-enriched

913   platforms, Zou *et al*. performed AFM topographical images and force mapping that allowed the

914   determination of the F_b value and elastic modulus of the different phases (Ruby May A Sullan et

915   al., 2009a, 2009b; Zou & Johnston, 2010). They confirmed the expulsion of cholesterol from

916   sphingolipid/Chol-enriched domains as a result of Cer incorporation, and observed an increased

917   mechanical stability attributed to the influence of Cer in the lipid organization and packing

918   behavior, also reported later on GalCer rich domains on model membranes with PC and Chol

919   (Berta Gumí-Audenis et al., 2015).

920   The group of Goñi has systematically explored the effect of the acyl compositions of

921   sphingomyelins and the corresponding ceramide counterparts in ternary mixtures with PC and

922   Chol (García-Arribas et al., 2016; González-Ramírez et al., 2019; Jiménez-Rojo et al., 2014)).

923   Combining confocal microscopy, DSC, AFM imaging and FS, they compared the effects of C24:1

924   Cer (nervonoyl ceramide, nCer) with those of C16:0 Cer (palmitoyl ceramide, pCer) in bilayers

925   composed basically of DOPC, SM (either C24:1, nSM or C16:0, pSM) and Chol (García-Arribas et

926   al., 2017). AFM-FS showed that nCer has a lower stiffening effect than pCer, while the presence

927   of nSM reduces the stiffness. When the proportion of phospholipid increases beyond 60 mol %,

928   a lateral phase separation occurs at the micrometer scale (González-Ramírez et al., 2019). The

929   authors interpreted this data as a pCer:Chol interaction, that would predominate at the lower

930   phospholipid concentrations. The putative pCer:Chol complexes (or nanodomains) would mix

931   well with the phospholipid. At higher SM concentrations pSM:pCer and pSM:Chol interactions

932   would become more important, giving rise to the coexisting s_o and l_o phases, respectively.

933   Heterogeneity, or lateral phase separation, occurs more easily with pSM than with DPPC,

934   indicating a higher affinity of SM over DPPC for Chol or Cer. Altogether, the findings of Goñi and

935   coworkers show the sharp increase in complexity when membranes exhibit different

936   sphingolipids of varying N-acyl chains, which should be a common issue in an actual cell

937   membrane environment.

938   ## 1.2. The role of cholesterol

939   Cholesterol is a fundamental constituent of the eukaryotic cell plasma membranes. Eukaryotic

940   cell membranes are not entirely in the conventional l_d phase. Instead, they are, at least partially,

941   in the Chol-rich liquid-ordered (l_o) phase or a phase with similar properties. l_o phase is

942 characterized by a high degree of acyl chain order and is favored by high-T_m lipids with saturated

943 acyl chains such as sphingolipids, when they are mixed with Chol, as exposed in the previous

944 section. Chol plays the essential function of regulating the physical properties of the cell

945 membrane as it controls the lipid organization and phase behavior, regulates the membrane

946 fluidity and its mechanical strength, influencing the passive permeability of water and other

947 small molecules (Pan et al., 2008; Pinkwart et al., 2019). From the molecular perspective, Chol

948 is considered to produce a condensing effect and induce ordering to fluid phase lipids forming

949 the membrane and to have the opposite effect on phospholipids present in the gel phase (Hung

950 et al., 2007; Rog et al., 2009). However, several experiments pointed out the complex effect of

951 Chol on lipid bilayers, which depends on the molecular structure of the neighboring lipids: the

952 degree of chain unsaturation, the length of the hydrophobic tail and the chemistry of the

953 headgroup (Pan et al., 2008; Mills et al., 2009; Garcia-Manyes et al., 2010). In view of

954 acknowledging the particular role of cholesterol, let us briefly outline results on the phase

955 behavior of SVLs and SLBs consisting of binary mixtures of saturated phospholipids and

956 cholesterol using mechanical descriptors such as shear viscosity of SVLs and nanomechanics of

957 SLBs.

958 We first describe the phase behavior of SVLs containing binary mixtures of DMPC:Chol using

959 QCM-D. Upon the addition of Chol to phospholipid bilayers, the sharp main phase transition in

960 pure DMPC gradually diminishes and eventually disappears over a given Chol concentration. In

961 the case of DMPC, SVLs showed no transition from 30% cholesterol. Figure 12 shows normalized

962 shear viscosity η_{norm} =[$\eta(t)/\eta(t=0)$, with t the time] for pure DMPC and DMPC:Chol (20 mol %

963 Chol) calculated using a Voigt-based viscoelastic model (Voinova et al., 1999). At intermediate

964 Chol concentrations, asymmetric peaks can be observed. These peaks encompass two main

965 contributions, a sharp, narrow peak and a broader one that overlaps with the former (see right

966 panel in Figure 12 for a more detailed view including Gaussian fitting). Two domains can be

967 identified, namely, the sharp contribution can be ascribed to the pure DMPC-rich domains

968 undergoing the main transition and the latter to the Chol-rich ones. The broader peak appears

969 as a result of the reduced mobility of the hydrophobic chains of DMPC in Chol-rich domains. The

970 presence and the size of these domains depend strongly on the concentration of cholesterol and

971 the temperature. On increasing the amount of cholesterol, the temperature range of the overall

972 transition increases as a result of the extension of the second broad contribution, while the size

973 of the maximum corresponding to the melting of the single lipid decreases. No phase transition

974 is detected at Chol concentration over 30 mol % indicating the formation of a homogeneous

975 liquid ordered l_o phase at a macroscopic level. Such a large cholesterol concentration inhibits

976   the formation of extended domains. A similar pattern of behavior was observed for DPPC:Chol

977   SVLs, however, for this later system, the completion temperature of the overall transition at

978   intermediate cholesterol concentrations was not attained, due to the (upper) limited

979   temperature range of commercial QCM-D systems (Losada-Pérez, Khorshid, et al., 2015). These

980   results are in agreement with recent calorimetric studies of free-standing membranes of the

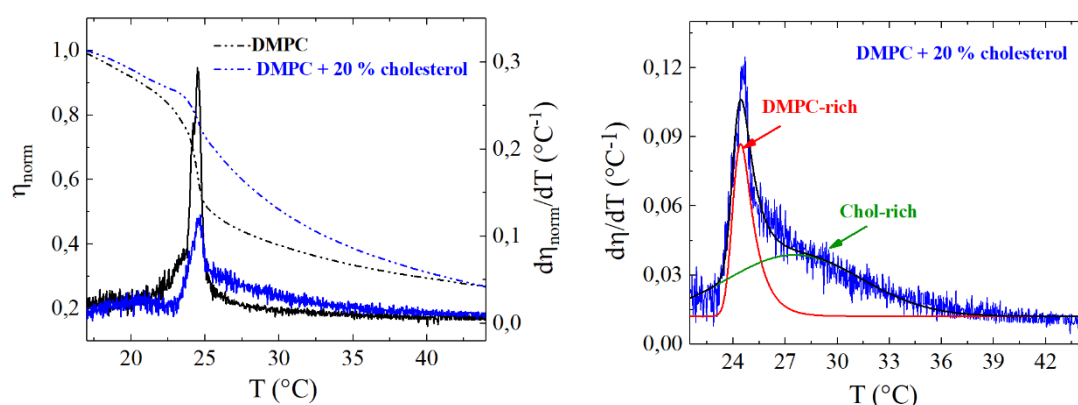981   same systems (Mannock et al., 2010).

982

983   **Figure 12.** Left panel Temperature dependence of the normalized effective shear viscosity (dash

984   dotted lines) and its first-order derivative (solid line) of DMPC and DMPC + 20% cholesterol SVLs

985   on a supported vesicle layer on a gold-coated QCM-D quartz sensor upon heating. Right panel

986   closer view of the normalized shear viscosity first-order derivative for DMPC + 20% cholesterol

987   SVLs. Solid lines denote multiple peak gaussian fitting.

988   The role of Chol in the structure and nanomechanics of SLBs has been extensively studied by

989   AFM (L Redondo-Morata et al., 2012b; R M A Sullan et al., 2010; Al-Rekabi & Contera, 2018; S

990   Garcia-Manyes et al., 2010; Adhyapak et al., 2018), as well as its interplay with sphingolipids or

991   other lipids (García-Arribas et al., 2016; 2006; Ahyayauch et al., 2002; Guyomarc'h et al., 2014)

992   and further reviewed in (B. Gumí-Audenis et al., 2016b).

993   By means of temperature-controlled AFM imaging and AFM-FS to assess the influence of Chol

994   on the membrane ordering and stability (Redondo-Morata et al., 2012), this work analyzed a

995   DPPC:Chol in representative range of compositions up to 50 mol % Chol, studying the phase

996   evolution upon heating (from room temperature to temperatures high above the T_m of DPPC)

997   and the corresponding (nano)mechanical stability. This provided a correlation between the

998   mechanical behavior and composition with the lateral order of each phase present in the

999   bilayers. It proved that low Chol contents lead to a phase segregated system, while high contents

1000   of Chol can give a homogeneous topography, although a bimodal F_b distribution was observed,

1001   possibly due to the presence of small heterogeneities that could not be resolved in the images.

1002   In all cases, it was demonstrated that Chol enhances the mechanical stability of the binary

1003   membrane, and an extraordinarily stable system was observed for equimolar fractions (50 mol

1004   % Chol). In addition, even when no thermal transition was detected by the traditional bulk

1005   analysis techniques for vesicles with high Chol content (40 and 50 mol %), it was shown that

1006   temperature-controlled AFM-FS is capable of identifying a thermal transition for the SLBs. As

1007   detailed in Figure 13, for high-Chol contents -40 and 50 mol %- the DPPC:Chol system shows a

1008   double F_b distribution at room temperature, probably due to the presence of (space or time)

1009   non-resolved heterogeneities for these compositions. Although no thermal transition was

1010   observed in DSC thermograms of free-standing systems, when AFM-FS experiments were

1011   performed at different temperatures for these systems, a gradual decrease of the mean F_b value

1012   was observed until temperature reached ca. 40 °C. The continuous decrease in the F_b value with

1013   increasing temperature may be ascribed to an increase in fluidity of the system, and it is evident

1014   that, although not detected in DSC of DPPC:Chol vesicles, a transition occurs for DPPC:Chol SLBs

1015   with 40 and 50 mol % Chol around 42-45 °C. Below this temperature, the system in the l_o phase

1016   presents extraordinary lateral order and may have properties that resemble a gel-like bilayer,

1017   and as temperature increases, it gradually becomes a system with higher lateral mobility (but

1018   still with higher order than the DPPC l_d phase). This behavior indicates that for DPPC:Chol SLBs,

1019   a thermal transition occurs even for high-Chol compositions, in a temperature range between

1020   ca. 42-47 °C independently of the membrane composition, and that it may probably be of

1021   second-order for the high-Chol DPPC:Chol bilayers (40-50 mol %), which generally appear as a

1022   very broad transition or it is even not detected in DSC experiments of free standing vesicles or
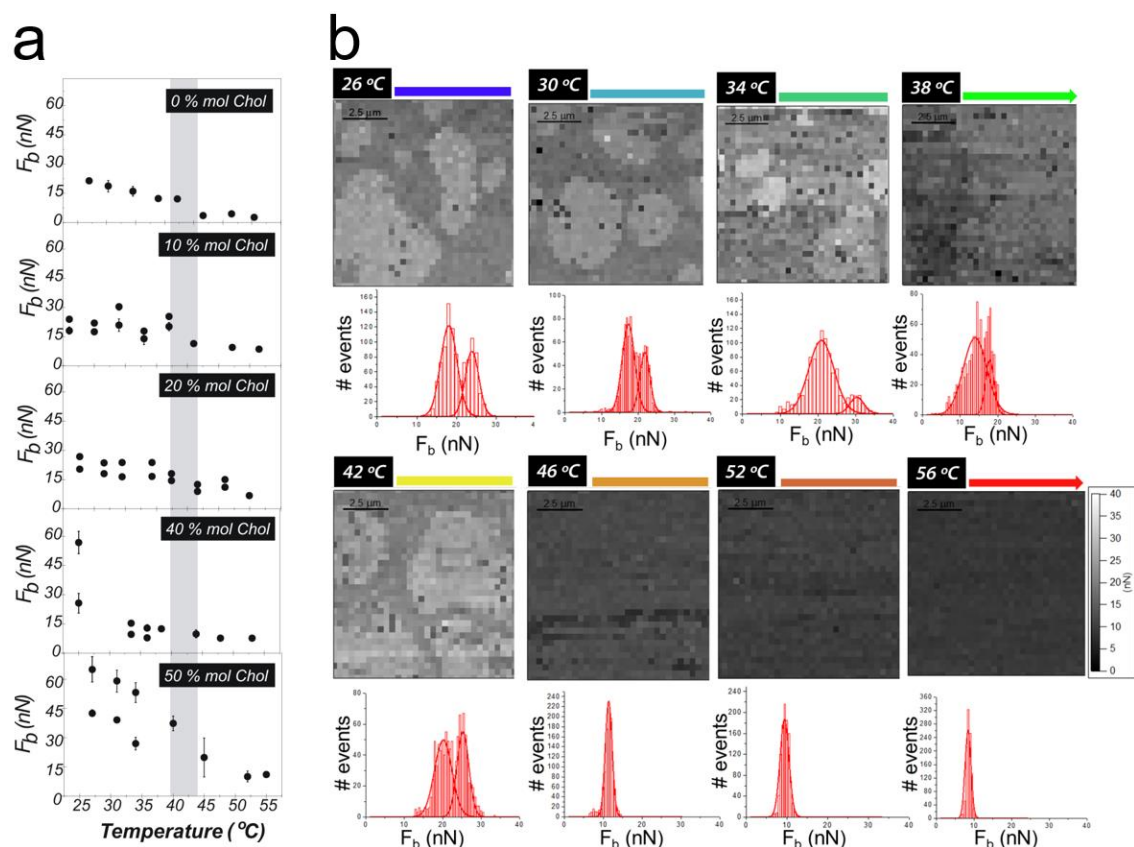
1023   QCM-D of SVLs.

Figure 13. a) Mean F_b value of DPPC:Chol SLBs in 10 mM HEPES, 20 mM MgCl$_2$ and 150 mM NaCl, pH 7.4, with various Chol contents, as a function of temperature. The shadowed vertical line marks the temperature range where the main transition in pure DPPC occurs. For DPPC:Chol SLBs with 40 and 50 mol % Chol, although not detected in DSC of DPPC:Chol vesicles, a transition occurs around 42–45 °C. b) F_b maps and distributions for DPPC:Chol SPB with 10 mol % Chol, in 10 mM HEPES, 20 mM MgCl$_2$ and 150 mM NaCl, pH 7.4, with increasing temperature. Reprinted from (L Redondo-Morata et al., 2012b).

Strikingly, information about the lateral in-plane structure of such systems can be instead obtained by grazing incidence XR diffraction (GIXD). In (Gumi-Audenis et al., 2018), a silicon-SLB system was designed in order to deal with the requirement of the wetting preservation to guarantee the membrane stability while minimizing the background from the liquid environment. Using this methodology, it was confirmed that DPPC:Chol with low contents of Chol up to 30 mol % lead to separation into two coexisting phases at room temperature and concentrations higher than 30 mol % Chol appear to be a unique l_o phase. This condition was consistent with the earlier work (Redondo-Morata et al., 2012b) demonstrating that such increase of nanomechanical resistance is associated to a strong lateral interaction mediated by Chol molecules placed between the DPPC ones, due to a highly stable structure with most probably an equimolar DPPC:Chol ratio.

1043 To date, efforts continue to understand the complex role of cholesterol in biomembranes. Still,

1044 these discoveries cannot always be directly translated to the behavior of living cell membranes.

1045 By means of advanced fluorescence imaging and spectroscopy, Sezgin and colleagues (Pinkwart

1046 et al., 2019) have shown that cholesterol diffuses faster than phospholipids in live membranes,

1047 but not in model membranes. Interestingly, a detailed statistical diffusion analysis suggested

1048 two-component diffusion for cholesterol in the plasma membrane of live cells.

1049 Recent work based on a systematic AFM-FS study on DOPC:Chol SLBs at varying ratios suggested,

1050 however, that cholesterol may not just be responsible of increasing the mechanical stability but

1051 also introduce irregularities across the leaflets (Adhyapak et al., 2018). At Chol ratios above 20%,

1052 they could observe two sudden jumps in the force-distance curve, the second jump always

1053 displaying shorten separation. They interpreted that cholesterol induced asymmetry across the

1054 (in the inner and outer leaflets) bilayer, related to the phenomena of interleaflet coupling and

1055 depending on Chol concentration.

1056 Recently, Contera and coworkers took a different approach to study the effect of Chol in the

1057 mechanical properties of lipid bilayers (Al-Rekabi & Contera, 2018). Applying different

1058 frequencies simultaneously in an AFM topography mode, namely amplitude modulation–

1059 frequency modulation (AM–FM), they investigated the effect of Chol on DPPC bilayers in

1060 concentrations from 0 to 60 %. The lipid bilayers probed with this methodology displayed both

1061 elastic and viscous behavior. Cholesterol showed to modulates both, increasing elastic and

1062 viscous components as a function of Chol concentrations. The authors interpreted that their

1063 results may have a physiological relevance, where such viscoelastic properties may be used by

1064 cells to modulate the propagation (elastic) or attenuation (viscous) of mechanical signals across

1065 the cell membrane.

1066 ## 5. Connection between nanoscale measurements and
1067 thermodynamic descriptors of membranes

1068

1069 When studying phase coexistence in lipid membranes a distinction between thermodynamically

1070 stable phases and transient local domains in lipid bilayer at equilibrium should be made. Let us

1071 briefly discuss this in line with the above-exposed results on phospholipid-cholesterol binary

1072 mixtures. PC-Chol binary mixtures have been studied for many years using a plethora of

1073 experimental techniques. Yet, despite their apparent simplicity being two-component systems,

1074 their phase behavior remains controversial and, in many cases, departs from the canonical phase

1075 diagram proposed by Vist and Davis (Vist & Davis, 1990). In fact, results depend strongly on the

1076 spatio-temporal resolution of the different experimental techniques. For instance, unlike

1077 predicted by most phase diagrams, l_d-l_o phase coexistence was not observed for micron-sized

1078 GUVs of DPPC-cholesterol mixtures using fluorescence microscopy (Veatch & Keller, 2003),

1079 while some other techniques captured this phenomenon for free standing MLVs vesicles (DSC

1080 (Mannock et al., 2010), volumetric (Miyoshi et al., 2014), NMR (Davis et al., 2009), SLBs (AFM)(L

1081 Redondo-Morata et al., 2012b), and SVLs (QCM-D)(Losada-Pérez, Khorshid, et al., 2015). These

1082 findings suggest that, instead of macroscopic phase separation, these systems are presumably

1083 filled with mesoscopic and nanoscopic domains, whose size and lifetime depends on

1084 temperature and mixture composition (Winkler et al., 2017).

1085 Classically, when dealing with phase separation the Gibbs' phase rule is customarily invoked,

1086 assuming macroscopic phase coexistence and neglecting the role of phase boundaries, which

1087 comparably, hardly contribute to the free energy. If domains are small, the interfaces between

1088 domains constitute an important part of the system and its contribution to the free energy is

1089 not negligible. In this respect, using the term phase in the classical thermodynamic sense might

1090 not be appropriate (Heimburg, 1998; Almeida et al., 2005). Following Hill (Hill, 2013) a system

1091 can no longer be called a phase when it ceases to behave like a macroscopic system and starts

1092 behaving like a small system.

1093 In this respect, both AFM and QCM-D have demonstrated to be valuable tools to detect domain

1094 (nano/mesoscopic sized domains) coexistence within supported membranes of binary lipid

1095 mixtures.

6. Conclusions and future perspectives

1096

1097 As mentioned in the previous sections, AFM-FS can interestingly resolve coexistence of domains

1098 at concentrations where height differences at domain boundaries are not detectable.

1099 Breakthrough force thus stands as a useful mechanical descriptor to resolve domain coexistence.

1100 Even though domains cannot be considered as phases in the purely thermodynamic standpoint,

1101 this does not mean that these systems cannot be treated in a rigorous thermodynamic way. As

1102 a matter of fact, the breakthrough force is able to detect a thermal transition at high cholesterol

1103 concentrations in binary PC:Chol SLBs, whose origin deserves to be revisited and further

1104 explored in the framework of either fluctuations arising in the vicinity of a critical point, the

1105 possibility of glassy-cholesterol-rich nanodomains or eventual cholesterol crystallization. In this

1106 sense, the development of HS-AFM will likely provide new insights due to its unprecedented

1107 spatio-temporal resolution, thanks to a direct correlation between structure and diffusion

1108 (Munguira et al., 2016). Similarly, HS Force Spectroscopy has the capacity to cover a wider force

1109   spectrum, which can help to validate theoretical frameworks of the field, as well as provide a

1110   direct correlation with Molecular Dynamics simulations (Rico et al., 2013).

1111   There is indeed plenty of room in fundamental lipid biophysics and phase behavior in particular

1112   to use both purely mechanical and viscoelastic properties as descriptors to provide a more

1113   complete picture of the origins of domain formation and coexistence. The ultimate lipid phase

1114   coexistence to be fully understood are transient nanodomains, often (confusively) referred to

1115   as lipid rafts. There is to date no agreement about the size and lifetime of rafts, and the term is

1116   used to referred to a collection of different structures (Goñi, 2019). Based on the current

1117   knowledge, microdomains in equilibrium are no longer considered suitable models for the

1118   biological structure that rafts represent. Fortunately, advanced super-resolution microscopies

1119   and fast techniques are becoming available and will shed some light in one of the most discussed

1120   topics in biomembrane studies.

1121   In light of this, multiscale spatio-temporal measurements of mechanical properties of supported

1122   membranes can help to experimentally address different scenarios where membrane micro- and

1123   nano-domain formation finds theoretical support. Starting from equilibrium ternary lipid

1124   mixtures in the vicinity of a critical point, it might be worth exploring how the presence of critical

1125   fluctuations reflects in the membrane mechanical properties, and if these properties can be

1126   used as physical descriptors to test critical-point universality laws. Secondly, tuning membrane

1127   (local and global) environment by actively controlling curvature, leaflet asymmetry, solid

1128   support topography and addition of external components would help complete the manifold

1129   where domain formation occurs. Finally, the growing spatiotemporal capabilities of AFM are

1130   promising tools to explore membrane organization in the realm of non-equilibrium phenomena.

1131   7. Acknowledgements

1138   8. Glossary of lipid acronyms

1139

Acronym	Long name

C16:0 palmitoyl Cer (aka palmitoyl Cer, pCer)	N-palmitoyl-D-erythro-sphingosine
C16:0 palmitoyl SM (aka palmitoyl SM)	N-palmitoyl-D-erythro-sphingosylphosphorylcholine
C24:1 nervonoyl Cer (aka nervonoyl Cer, nCer)	N-nervonoyl-D-erythro-sphingosine
C24:1 nervonoyl SM (aka nervonoyl SM)	N-Nervonoyl-D-erythro-sphingosylphosphorylcholine-d9
Cer	ceramide
Chol	cholesterol
CL	cardiolipin
DMPC	1,2-dimyristoyl-sn-glycero-3-phosphocholine
DOPC	1,2-dioleoyl-sn-glycero-3-phosphocholine
DOPE	1,2-dioleoyl-sn-glycero-3-phosphoethanolamine
DOPG	1,2-dioleoyl-sn-glycero-3-[phospho-rac-(3-lysyl(1-glycerol))]
DOTAP	1,2-dioleoyl-3-trimethylammonium-propane
DPPA	1,2-dipalmitoyl-sn-glycero-3-phosphate
DPPC	1,2-dipalmitoyl-sn-glycero-3-phosphocholine
DPPE	1,2-dipalmitoyl-sn-glycero-3-phosphoethanolamine
DPPG	1,2-dipalmitoyl-sn-glycero-3-phospho-(1'-rac-glycerol)
DSPC	1,2-distearoyl-sn-glycero-3-phosphocholine
GalCer	Galactosylceramides
PC	phosphocholine
PE	phosphoethanolamine
POPC	1-palmitoyl-2-oleoyl-glycero-3-phosphocholine
POPE	1-palmitoyl-2-oleoyl-sn-glycero-3-phosphoethanolamine
POPG	1-palmitoyl-2-oleoyl-sn-glycero-3-phospho-(1'-rac-glycerol)
SM	sphongomyelin

9. References

1142   Adhyapak, P. R., Panchal, S. V., & Murthy, A. V. R. (2018). Cholesterol induced asymmetry in

1143   DOPC bilayers probed by AFM force spectroscopy. *Biochimica et Biophysica Acta (BBA)*

1144   *- Biomembranes*, *1860*(5), 953–959. https://doi.org/10.1016/j.bbamem.2018.01.021

1145   Ahyayauch, H., Requero, M. A., Alonso, A., Bennouna, M., & Goni, F. M. (2002). Surfactant

1146   effects of chlorpromazine and imipramine on lipid bilayers containing sphingomyelin

1147   and cholesterol. *Journal of Colloid and Interface Science*, *256*(2), 284–289.

1148   https://doi.org/10.1006/jcis.2002.8690

1149   Alessandrini, A., & Facci, P. (2012). Nanoscale mechanical properties of lipid bilayers and their

1150   relevance in biomembrane organization and function. *Micron*, *43*(12), 1212–1223.

1151   https://doi.org/10.1016/j.micron.2012.03.013

1152   Almeida, P. F. F., Pokorny, A., & Hinderliter, A. (2005). Thermodynamics of membrane

1153   domains. *Biochimica et Biophysica Acta (BBA) - Biomembranes*, *1720*(1), 1–13.

1154   https://doi.org/10.1016/j.bbamem.2005.12.004

1155   Al-Rekabi, Z., & Contera, S. (2018). Multifrequency AFM reveals lipid membrane mechanical

1156   properties and the effect of cholesterol in modulating viscoelasticity. *Proceedings of*

1157   *the National Academy of Sciences*, *115*(11), 2658–2663.

1158   https://doi.org/10.1073/pnas.1719065115

1159   Ando, T, Uchihashi, T., Kodera, N., Yamamoto, D., Miyagi, A., Taniguchi, M., & Yamashita, H.

1160   (2008). High-speed AFM and nano-visualization of biomolecular processes. *Pflugers*

1161   *Archiv-European Journal of Physiology*, *456*(1), 211–225.

1162   https://doi.org/10.1007/s00424-007-0406-0

1163   Ando, Toshio. (2017). High-speed atomic force microscopy and its future prospects. *Biophysical*

1164   *Reviews*, *10*(2), 285–292. https://doi.org/10.1007/s12551-017-0356-5

1165   Armond, J. W., Macpherson, J. V, & Turner, M. S. (2011). Pulling Nanotubes from Supported

1166   Bilayers. *Langmuir*, *27*(13), 8269–8274.

1167   Bangham, A. D., & Horne, R. W. (1964). Negative staining of phospholipids and their structural

1168   modification by surface-active agents as observed in the electron microscope. *Journal*

1169   *of Molecular Biology*, *8*(5), 660-IN10. https://doi.org/10.1016/S0022-2836(64)80115-7

1170   BANGHAM, A. D., PETHICA, B. A., & SEAMAN, G. V. (1958). The charged groups at the interface

1171   of some blood cells. *The Biochemical Journal*, *69*(1), 12–19.

1172   https://doi.org/10.1042/bj0690012

1173   Barrett, R. C. (1991). High-speed, large-scale imaging with the atomic force microscope.

1174   *Journal of Vacuum Science & Technology B: Microelectronics and Nanometer*

1175   *Structures*, *9*(2), 302. https://doi.org/10.1116/1.585610

1176   Berg, J. M., Tymoczko, J. L., Stryer, L., Berg, J. M., Tymoczko, J. L., & Stryer, L. (2002).

1177   *Biochemistry* (5th ed.). W H Freeman.

1178   Bernchou, U., Ipsen, J. H., & Simonsen, A. C. (2009). Growth of solid domains in model

1179   membranes: Quantitative image analysis reveals a strong correlation between domain

1180   shape and spatial position. *The Journal of Physical Chemistry. B*, *113*(20), 7170–7177.

1181   https://doi.org/10.1021/jp809989t

1182   Binnig, G., Quate, C. F., & Gerber, C. (1986). ATOMIC FORCE MICROSCOPE. *Physical Review*

1183   *Letters*, *56*(9), 930–933. https://doi.org/10.1103/PhysRevLett.56.930

1184   Blanchette, C. D., Lin, W.-C., Ratto, T. V., & Longo, M. L. (2006). Galactosylceramide Domain

1185   Microstructure: Impact of Cholesterol and Nucleation/Growth Conditions. *Biophysical*

1186   *Journal*, *90*(12), 4466–4478. https://doi.org/10.1529/biophysj.105.072744

1187   Brochard-Wyart, F., Borghi, N., Cuvelier, D., & Nassoy, P. (2006). Hydrodynamic narrowing of

1188   tubes extruded from cells. *Proceedings of the National Academy of Sciences*, *103*(20),

1189   7660.

1190   Butt, H. J., & Franz, V. (2002). Rupture of molecular thin films observed in atomic force

1191   microscopy. I. Theory. *Physical Review E*, *66*(3).

1192   https://doi.org/10.1103/PhysRevE.66.031601

1193   Canham, P. B. (1970). The minimum energy of bending as a possible explanation of the

1194   biconcave shape of the human red blood cell. *Journal of Theoretical Biology*, *26*(1), 61–

1195   81.

1196   Chiantia, S, Kahya, N., Ries, J., & Schwille, P. (2006). Effects of ceramide on liquid-ordered

1197   domains investigated by simultaneous AFM and FCS. *Biophysical Journal*, *90*(12),

1198   4500–4508. https://doi.org/10.1529/biophysj.106.081026

Chiantia, S, Ries, J., Kahya, N., & Schwille, P. (2006). Combined AFM and two-focus SFCS study of raft-exhibiting model membranes. *Chemphyschem*, *7*(11), 2409–2418. https://doi.org/10.1002/cphc.200600464

Chiantia, Salvatore, Kahya, N., & Schwille, P. (2007). Raft domain reorganization driven by short- and long-chain ceramide: A combined AFM and FCS study. *Langmuir*, *23*(14), 7659–7665. https://doi.org/10.1021/la7010919

Chiantia, Salvatore, Ries, J., Chwastek, G., Carrer, D., Li, Z., Bittman, R., & Schwille, P. (2008). Role of ceramide in membrane protein organization investigated by combined AFM and FCS. *Biochimica Et Biophysica Acta-Biomembranes*, *1778*(5), 1356–1364. https://doi.org/10.1016/j.bbamem.2008.02.008

Chiaruttini, N., Redondo-Morata, L., Colom, A., Humbert, F., Lenz, M., Scheuring, S., & Roux, A. (2015). Relaxation of Loaded ESCRT-III Spiral Springs Drives Membrane Deformation. *Cell*, *163*(4), 866–879. https://doi.org/10.1016/j.cell.2015.10.017

Cho, N.-J., Frank, C. W., Kasemo, B., & Höök, F. (2010). Quartz crystal microbalance with dissipation monitoring of supported lipid bilayers on various substrates. *Nature Protocols*, *5*(6), 1096–1106. https://doi.org/10.1038/nprot.2010.65

Cho, N.-J., Kanazawa, K. K., Glenn, J. S., & Frank, C. W. (2007). Employing Two Different Quartz Crystal Microbalance Models To Study Changes in Viscoelastic Behavior upon Transformation of Lipid Vesicles to a Bilayer on a Gold Surface. *Analytical Chemistry*, *79*(18), 7027–7035. https://doi.org/10.1021/ac0709504

Choi, S.-E., Greben, K., Wördenweber, R., & Offenhäusser, A. (2016). Positively charged supported lipid bilayer formation on gold surfaces for neuronal cell culture. *Biointerphases*, *11*(2), 21003. https://doi.org/10.1116/1.4945306

Clausen-Schaumann, H., Rief, M., Tolksdorf, C., & Gaub, H. E. (2000). Mechanical stability of single DNA molecules. *Biophysical Journal*, *78*(4), 1997–2007.

_____

1224   Crespo-Villanueva, A., Gumí-Audenis, B., Sanz, F., Artzner, F., Mériadec, C., Rousseau, F., Lopez,

1225   C., Giannotti, M. I., & Guyomarc'h, F. (2018). Casein interaction with lipid membranes:

1226   Are the phase state or charge density of the phospholipids affecting protein

1227   adsorption? *Biochimica Et Biophysica Acta. Biomembranes*, *1860*(12), 2588–2598.

1228   https://doi.org/10.1016/j.bbamem.2018.09.016

1229   Dai, J., & Sheetz, M. P. (1999). Membrane Tether Formation from Blebbing Cells. *Biophysical*

1230   *Journal*, *77*(6), 3363–3370.

1231   Daillant, J., Bellet-Amalric, E., Braslau, A., Charitat, T., Fragneto, G., Graner, F., Mora, S.,

1232   Rieutord, F., & Stidder, B. (2005). Structure and fluctuations of a single floating lipid

1233   bilayer. *Proceedings of the National Academy of Sciences of the United States of*

1234   *America*, *102*(33), 11639.

1235   Davis, J. H., Clair, J. J., & Juhasz, J. (2009). Phase Equilibria in DOPC/DPPC-d62/Cholesterol

1236   Mixtures. *Biophysical Journal*, *96*(2), 521–539.

1237   https://doi.org/10.1016/j.bpj.2008.09.042

1238   Deamer, D. W. (2010). From "banghasomes" to liposomes: A memoir of Alec Bangham, 1921-

1239   2010. *The FASEB Journal : Official Publication of the Federation of American Societies*

1240   *for Experimental Biology*, *24*(5), 1308–1310. https://doi.org/10.1096/fj.10-0503

1241   Dieluweit, S., Csiszar, A., Rubner, W., Fleischhauer, J., Houben, S., & Merkel, R. (2010).

1242   Mechanical Properties of Bare and Protein-Coated Giant Unilamellar Phospholipid

1243   Vesicles. A Comparative Study of Micropipet Aspiration and Atomic Force Microscopy.

1244   *Langmuir*, *26*(13), 11041–11049. https://doi.org/10.1021/la1005242

1245   Dimova, R. (2019). Giant Vesicles and Their Use in Assays for Assessing Membrane Phase State,

1246   Curvature, Mechanics, and Electrical Properties. *Annual Review of Biophysics*, *48*(1),

1247   93–119. https://doi.org/10.1146/annurev-biophys-052118-115342

1248   Doktorova, M., Heberle, F. A., Eicher, B., Standaert, R. F., Katsaras, J., London, E., Pabst, G., &

1249   Marquardt, D. (2018). Preparation of asymmetric phospholipid vesicles for use as cell

1250   membrane models. *Nature Protocols*, *13*(9), 2086–2101.

1251   https://doi.org/10.1038/s41596-018-0033-6

1252   Domenech, O., Redondo, L., Picas, L., Morros, A., Montero, M. T., & Hernandez-Borrell, J.

1253   (2007). Atomic force microscopy characterization of supported planar bilayers that

1254   mimic the mitochondrial inner membrane. *Journal of Molecular Recognition*, *20*(6),

1255   546–553. https://doi.org/10.1002/jmr.849

1256   Dufrêne, Y. F., Ando, T., Garcia, R., Alsteens, D., Martinez-Martin, D., Engel, A., Gerber, C., &

1257   Müller, D. J. (2017). Imaging modes of atomic force microscopy for application in

1258   molecular and cell biology. *Nature Nanotechnology*, *12*, 295.

1259   https://doi.org/10.1038/nnano.2017.45

1260   Dufrene, Y. F., Barger, W. R., Green, J. B. D., & Lee, G. U. (1997). Nanometer-scale surface

1261   properties of mixed phospholipid monolayers and bilayers. *Langmuir*, *13*(18), 4779–

1262   4784. https://doi.org/10.1021/la970221r

1263   Dufrene, Y. F., Boland, T., Schneider, J. W., Barger, W. R., & Lee, G. U. (1998). Characterization

1264   of the physical properties of model biomembranes at the nanometer scale with the

1265   atomic force microscope. *Faraday Discussions*, *111*, 79–94.

1266   Dufrêne, Y. F., & Lee, G. U. (2000). Advances in the characterization of supported lipid films

1267   with the atomic force microscope. *Biochimica et Biophysica Acta (BBA) -*

1268   *Biomembranes*, *1509*(1), 14–41. https://doi.org/10.1016/S0005-2736(00)00346-1

1269   Ehrig, J., Petrov, E. P., & Schwille, P. (2011). Phase separation and near-critical fluctuations in

1270   two-component lipid membranes: Monte Carlo simulations on experimentally relevant

1271   scales. *New Journal of Physics*, *13*(4), 045019. https://doi.org/10.1088/1367-

1272   2630/13/4/045019

1273   El Kirat, K., Morandat, S., & Dufrene, Y. F. (2010). Nanoscale analysis of supported lipid bilayers

1274   using atomic force microscopy. *Biochimica Et Biophysica Acta-Biomembranes*, *1798*(4),

1275   750–765. https://doi.org/10.1016/j.bbamem.2009.07.026

1276   Evans, E, & Ritchie, K. (1997). Dynamic strength of molecular adhesion bonds. *Biophysical*

1277   *Journal*, *72*(4), 1541–1555.

1278   Evans, E, & Yeung, A. (1994). Hidden dynamics in rapid changes of bilayer shape. *Chemistry and*

1279   *Physics of Lipids*, *73*(1), 39–56. https://doi.org/10.1016/0009-3084(94)90173-2

1280   Evans, Evan, Heinrich, V., Ludwig, F., & Rawicz, W. (2003). Dynamic Tension Spectroscopy and

1281   Strength of Biomembranes. *Biophysical Journal*, *85*(4), 2342–2350.

1282   Fidorra, M., Heimburg, T., & Seeger, H. M. (2009). Melting of individual lipid components in

1283   binary lipid mixtures studied by FTIR spectroscopy, DSC and Monte Carlo simulations.

1284   *Biochimica Et Biophysica Acta-Biomembranes*, *1788*(3), 600–607.

1285   https://doi.org/10.1016/j.bbamem.2008.12.003

1286   Florin, E. L., Moy, V. T., & Gaub, H. E. (1994). Adhesion forces between individual ligand-

1287   receptor pairs. *Science*, *264*(5157), 415 LP – 417.

1288   https://doi.org/10.1126/science.8153628

1289   Franz, V., Loi, S., Muller, H., Bamberg, E., & Butt, H. H. (2002). Tip penetration through lipid

1290   bilayers in atomic force microscopy. *Colloids and Surfaces B-Biointerfaces*, *23*(2–3),

1291   191–200.

1292   García-Arribas, A. B., Alonso, A., & Goñi, F. M. (2016). Cholesterol interactions with ceramide

1293   and sphingomyelin. *Chemistry and Physics of Lipids*, *199*, 26–34.

1294   https://doi.org/10.1016/j.chemphyslip.2016.04.002

1295   García-Arribas, A. B., González-Ramírez, E. J., Sot, J., Areso, I., Alonso, A., & Goñi, F. M. (2017).

1296   Complex Effects of 24:1 Sphingolipids in Membranes Containing

1297   Dioleoylphosphatidylcholine and Cholesterol. *Langmuir*, *33*(22), 5545–5554.

1298   https://doi.org/10.1021/acs.langmuir.7b00162

1299   Garcia-Manyes, S, Guell, A. G., Gorostiza, P., & Sanz, F. (2005). Nanomechanics of silicon

1300   surfaces with atomic force microscopy: An insight to the first stages of plastic

1301   deformation. *Journal of Chemical Physics*, *123*(11). https://doi.org/10.1063/1.2035094

1302   Garcia-Manyes, S, Oncins, G., & Sanz, F. (2005a). Effect of ion-binding and chemical

1303   phospholipid structure on the nanomechanics of lipid bilayers studied by force

1304   spectroscopy. *Biophysical Journal*, *89*, 1812–1826.

1305   https://doi.org/10.1529/biophysj.105.064030

1306   Garcia-Manyes, S, Oncins, G., & Sanz, F. (2005b). Effect of temperature on the nanomechanics

1307   of lipid bilayers studied by force spectroscopy. *Biophysical Journal*, *89*(6), 4261–4274.

1308   https://doi.org/10.1529/biophysj.105.065581

1309   Garcia-Manyes, S, Redondo-Morata, L., Oncins, G., & Sanz, F. (2010). Nanomechanics of Lipid

1310   Bilayers: Heads or Tails? *Journal of the American Chemical Society*, *132*(37), 12874–

1311   12886. https://doi.org/10.1021/ja1002185

1312   Garcia-Manyes, S, & Sanz, F. (2010). Nanomechanics of lipid bilayers by force spectroscopy

1313   with AFM: A perspective. *Biochimica Et Biophysica Acta-Biomembranes*, *1798*(4), 741–

1314   749. https://doi.org/10.1016/j.bbamem.2009.12.019

1315   Garcia-Manyes, Sergi, Redondo-Morata, L., Oncins, G., & Sanz, F. (2010). Nanomechanics of

1316   Lipid Bilayers: Heads or Tails? *Journal of the American Chemical Society*, *132*(37),

1317   12874–12886. https://doi.org/10.1021/ja1002185

1318   Giannotti, M. I., & Vancso, G. J. (2007). Interrogation of single synthetic polymer chains and

1319   polysaccharides by AFM-based force spectroscopy. *ChemPhysChem*, *8*(16).

1320   https://doi.org/10.1002/cphc.200700175

1321   Giles, R., Cleveland, J. P., Manne, S., Hansma, P. K., Drake, B., Maivald, P., Boles, C., Gurley, J.,

1322   & Elings, V. (1993). Noncontact force microscopy in liquids. *Applied Physics Letters*,

1323   *63*(5), 617–618. https://doi.org/10.1063/1.109967

1324   Gillissen, J. J. J., Jackman, J. A., Tabaei, S. R., Yoon, B. K., & Cho, N.-J. (2017). Quartz Crystal

1325   Microbalance Model for Quantitatively Probing the Deformation of Adsorbed Particles

1326   at Low Surface Coverage. *Analytical Chemistry*, *89*(21), 11711–11718.

1327   https://doi.org/10.1021/acs.analchem.7b03179

1328 Goñi, F. M. (2019a). "Rafts": A nickname for putative transient nanodomains. *Chemistry and*

1329   *Physics of Lipids*, *218*, 34–39. https://doi.org/10.1016/j.chemphyslip.2018.11.006

1330 Goñi, F. M. (2019b). "Rafts": A nickname for putative transient nanodomains. In *Chemistry and*

1331   *Physics of Lipids* (Vol. 218, pp. 34–39). Elsevier Ireland Ltd.

1332   https://doi.org/10.1016/j.chemphyslip.2018.11.006

1333 González-Ramírez, E. J., Artetxe, I., García-Arribas, A. B., Goñi, F. M., & Alonso, A. (2019).

1334   Homogeneous and Heterogeneous Bilayers of Ternary Lipid Compositions Containing

1335   Equimolar Ceramide and Cholesterol. *Langmuir*, *35*(15), 5305–5315.

1336   https://doi.org/10.1021/acs.langmuir.9b00324

1337 Gumí-Audenis, B., Costa, L., Carlá, F., Comin, F., Sanz, F., & Giannotti, M. I. (2016a). Structure

1338   and nanomechanics of model membranes by atomic force microscopy and

1339   spectroscopy: Insights into the role of cholesterol and sphingolipids. *Membranes*, *6*(4).

1340   https://doi.org/10.3390/membranes6040058

1341 Gumí-Audenis, B., Costa, L., Carlá, F., Comin, F., Sanz, F., & Giannotti, M. I. (2016b). Structure

1342   and nanomechanics of model membranes by atomic force microscopy and

1343   spectroscopy: Insights into the role of cholesterol and sphingolipids. *Membranes*, *6*(4).

1344   https://doi.org/10.3390/membranes6040058

1345 Gumí-Audenis, B., Costa, L., Redondo-Morata, L., Milhiet, P.-E., Sanz, F., Felici, R., Giannotti, M.

1346   I., & Carlà, F. (2018). In-plane molecular organization of hydrated single lipid bilayers:

1347   DPPC: cholesterol. *Nanoscale*, *10*(1). https://doi.org/10.1039/c7nr07510c

1348 Gumi-Audenis, B., Costa, L., Redondo-Morata, L., Milhiet, P.-E., Sanz, F., Felici, R., Giannotti, M.

1349   I., & Carla, F. (2018). In-plane molecular organization of hydrated single lipid bilayers:

1350   DPPC:cholesterol. *Nanoscale*, *10*(1), 87–92. https://doi.org/10.1039/c7nr07510c

1351 Gumí-Audenis, Berta, Costa, L., Ferrer-Tasies, L., Ratera, I., Ventosa, N., Sanz, F., & Giannotti,

1352   M. I. (2018). Pulling lipid tubes from supported bilayers unveils the underlying

1353 substrate contribution to the membrane mechanics. *Nanoscale*.

1354 https://doi.org/10.1039/C8NR03249A

1355 Gumí-Audenis, Berta, Sanz, F., & Giannotti, M. I. (2015). Impact of galactosylceramides on the

1356 nanomechanical properties of lipid bilayer models: An AFM-force spectroscopy study.

1357 *Soft Matter*, *11*(27), 5447–5454. https://doi.org/10.1039/C5SM01252J

1358 Guyomarc'h, F., Zou, S., Chen, M., Milhiet, P.-E., Godefroy, C., Vié, V., & Lopez, C. (2014). Milk

1359 Sphingomyelin Domains in Biomimetic Membranes and the Role of Cholesterol:

1360 Morphology and Nanomechanical Properties Investigated Using AFM and Force

1361 Spectroscopy. *Langmuir*, *30*(22), 6516–6524. https://doi.org/10.1021/la501640y

1362 Hardy, G. J., Nayak, R., & Zauscher, S. (2013). Model cell membranes: Techniques to form

1363 complex biomimetic supported lipid bilayers via vesicle fusion. *Current Opinion in*

1364 *Colloid & Interface Science*, *18*(5), 448–458.

1365 https://doi.org/10.1016/j.cocis.2013.06.004

1366 Hasan, I. Y., & Mechler, A. (2015). Viscoelastic changes measured in partially suspended single

1367 bilayer membranes. *Soft Matter*, *11*(27), 5571–5579.

1368 https://doi.org/10.1039/C5SM00278H

1369 Hassinger, J. E., Oster, G., Drubin, D. G., & Rangamani, P. (2017). Design principles for robust

1370 vesiculation in clathrin-mediated endocytosis. *Proceedings of the National Academy of*

1371 *Sciences*, *114*(7), E1118 LP-E1127. https://doi.org/10.1073/pnas.1617705114

1372 Heimburg, T. (1998). Mechanical aspects of membrane thermodynamics. Estimation of the

1373 mechanical properties of lipid membranes close to the chain melting transition from

1374 calorimetry. *Biochimica Et Biophysica Acta-Biomembranes*, *1415*(1), 147–162.

1375 https://doi.org/10.1016/s0005-2736(98)00189-8

1376 Hill, T. L. (2013). *Thermodynamics of Small Systems/* (Reprint). Dover Publications Inc.

1377   Hochmuth, F. M., Shao, J. Y., Dai, J., & Sheetz, M. P. (1996). Deformation and flow of

1378   membrane into tethers extracted from neuronal growth cones. *Biophysical Journal*,

1379   *70*(1), 358–369.

1380   Hohner, A. O., David, M. P. C., & Rädler, J. O. (2010). Controlled solvent-exchange deposition of

1381   phospholipid membranes onto solid surfaces. *Biointerphases*, *5*(1), 1–8.

1382   https://doi.org/10.1116/1.3319326

1383   Hugel, T., & Seitz, M. (2001). The Study of Molecular Interactions by AFM Force Spectroscopy.

1384   *Macromolecular Rapid Communications*, *22*(13), 989–1016.

1385   https://doi.org/10.1002/1521-3927(20010901)22:13<989::AID-MARC989>3.0.CO;2-D

1386   Hung, W.-C., Lee, M.-T., Chen, F.-Y., & Huang, H. W. (2007). The condensing effect of

1387   cholesterol in lipid bilayers. *Biophysical Journal*, *92*(11), 3960–3967.

1388   https://doi.org/10.1529/biophysj.106.099234

1389   Hurley, J. H., Boura, E., Carlson, L.-A., & Rózycki, B. (2010). Membrane Budding. *Cell*, *143*(6),

1390   875–887. https://doi.org/10.1016/j.cell.2010.11.030

1391   Ira, Zou, S., Ramirez, D. M. C., Vanderlip, S., Ogilvie, W., Jakubek, Z. J., & Johnston, L. J. (2009).

1392   Enzymatic generation of ceramide induces membrane restructuring: Correlated AFM

1393   and fluorescence imaging of supported bilayers. *Journal of Structural Biology*, *168*(1),

1394   78–89. https://doi.org/10.1016/j.jsb.2009.03.014

1395   Jiménez-Rojo, N., García-Arribas, A. B., Sot, J., Alonso, A., & Goñi, F. M. (2014). Lipid bilayers

1396   containing sphingomyelins and ceramides of varying N-acyl lengths: A glimpse into

1397   sphingolipid complexity. *Biochimica et Biophysica Acta - Biomembranes*, *1838*(1

1398   PARTB), 456–464. https://doi.org/10.1016/j.bbamem.2013.10.010

1399   Jing, Y., Trefna, H., Persson, M., Kasemo, B., & Svedhem, S. (2013). Formation of supported

1400   lipid bilayers on silica: Relation to lipid phase transition temperature and liposome

1401   size. *Soft Matter*, *10*(1), 187–195. https://doi.org/10.1039/C3SM50947H

1402   Johnston, L. J. (2007). Nanoscale imaging of domains in supported lipid membranes. *Langmuir:*

1403   *The ACS Journal of Surfaces and Colloids*, *23*(11), 5886–5895.

1404   https://doi.org/10.1021/la070108t

1405   Kahya, N., Scherfeld, D., Bacia, K., & Schwille, P. (2004). Lipid domain formation and dynamics

1406   in giant unilamellar vesicles explored by fluorescence correlation spectroscopy. *Journal*

1407   *of Structural Biology*, *147*(1), 77–89. https://doi.org/10.1016/j.jsb.2003.09.021

1408   Kechagia, J. Z., Ivaska, J., & Roca-Cusachs, P. (2019). Integrins as biomechanical sensors of the

1409   microenvironment. *Nature Reviews Molecular Cell Biology*, *20*(8), 457–473.

1410   https://doi.org/10.1038/s41580-019-0134-2

1411   Keller, C. A., & Kasemo, B. (1998). Surface specific kinetics of lipid vesicle adsorption measured

1412   with a quartz crystal microbalance. *Biophysical Journal*, *75*(3), 1397–1402.

1413   Keller, D., Larsen, N. B., Moller, I. M., & Mouritsen, O. G. (2005). Decoupled phase transitions

1414   and grain-boundary melting in supported phospholipid bilayers. *Physical Review*

1415   *Letters*, *94*(2). https://doi.org/10.1103/PhysRevLett.94.025701

1416   Kodera, N., Yamamoto, D., Ishikawa, R., & Ando, T. (2010). Video imaging of walking myosin V

1417   by high-speed atomic force microscopy. *Nature*, *468*(7320).

1418   https://doi.org/10.1038/nature09450

1419   Kurniawan, J., Ventrici de Souza, J. F., Dang, A. T., Liu, G., & Kuhl, T. L. (2018). Preparation and

1420   Characterization of Solid-Supported Lipid Bilayers Formed by Langmuir–Blodgett

1421   Deposition: A Tutorial. *Langmuir*, *34*(51), 15622–15639.

1422   https://doi.org/10.1021/acs.langmuir.8b03504

1423   Lee, G. U., Chrisey, L. A., & Colton, R. J. (1994). DIRECT MEASUREMENT OF THE FORCES

1424   BETWEEN COMPLEMENTARY STRANDS OF DNA. *Science*, *266*(5186), 771–773.

1425   https://doi.org/10.1126/science.7973628

1426   Leonenko, Z. V, Finot, E., Ma, H., Dahms, T. E. S., & Cramb, D. T. (2004). Investigation of

1427   temperature-induced phase transitions in DOPC and DPPC phospholipid bilayers using

1428   temperature-controlled scanning force microscopy. *Biophysical Journal*, *86*(6), 3783–

1429   3793. https://doi.org/10.1529/biophysj.103.036681

1430 Leonenko, Z. V., Finot, E., Ma, H., Dahms, T. E. S., & Cramb, D. T. (2004). Investigation of

1431   temperature-induced phase transitions in DOPC and DPPC phospholipid bilayers using

1432   temperature-controlled scanning force microscopy. *Biophysical Journal*, *86*(6), 3783–

1433   3793. https://doi.org/10.1529/biophysj.103.036681

1434 Lin, D. C., Dimitriadis, E. K., & Horkay, F. (2007). Robust strategies for automated AFM force

1435   curve analysis—I. Non-adhesive indentation of soft, inhomogeneous materials. *Journal*

1436   *of Biomechanical Engineering*, *129*(3), 430–440. https://doi.org/10.1115/1.2720924

1437 Lin, W.-C., Blanchette, C. D., & Longo, M. L. (2007). Fluid-Phase Chain Unsaturation Controlling

1438   Domain Microstructure and Phase in Ternary Lipid Bilayers Containing GalCer and

1439   Cholesterol. *Biophysical Journal*, *92*(8), 2831–2841.

1440   https://doi.org/10.1529/biophysj.106.095422

1441 Lind, T. K., & Cárdenas, M. (2016). Understanding the formation of supported lipid bilayers via

1442   vesicle fusion-A case that exemplifies the need for the complementary method

1443   approach (Review). *Biointerphases*, *11*(2), 020801. https://doi.org/10.1116/1.4944830

1444 Lipowsky, R., & Seifert, U. (1991). Adhesion of Vesicles and Membranes. *Molecular Crystals*

1445   *and Liquid Crystals*, *202*(1), 17–25. https://doi.org/10.1080/00268949108035656

1446 Loi, S, Sun, G., Franz, V., & Butt, H. J. (2002). Rupture of molecular thin films observed in

1447   atomic force microscopy. II. Experiment. *Physical Review E*, *66*(3).

1448   https://doi.org/031602 10.1103/PhysRevE.66.031602

1449 Loi, Simona, Sun, G., Franz, V., & Butt, H.-J. (2002). Rupture of molecular thin films observed in

1450   atomic force microscopy. II. Experiment. *Phys Rev E Stat Nonlin Soft Matter Phys*, *66*(3

1451   Pt 1), 31602.

1452 Losada-Pérez, P., Jiménez-Monroy, K. L., Grinsven, B. van, Leys, J., Janssens, S. D., Peeters, M.,

1453   Glorieux, C., Thoen, J., Haenen, K., Ceuninck, W. D., & Wagner, P. (2014). Phase

1454   transitions in lipid vesicles detected by a complementary set of methods: Heat-transfer

1455   measurements, adiabatic scanning calorimetry, and dissipation-mode quartz crystal

1456   microbalance. *Physica Status Solidi (a)*, *211*(6), 1377–1388.

1457   https://doi.org/10.1002/pssa.201431060

1458   Losada-Pérez, P., Khorshid, M., Yongabi, D., & Wagner, P. (2015). Effect of Cholesterol on the

1459   Phase Behavior of Solid-Supported Lipid Vesicle Layers. *The Journal of Physical*

1460   *Chemistry B*, *119*(15), 4985–4992. https://doi.org/10.1021/acs.jpcb.5b00712

1461   Losada-Pérez, P., Mertens, N., de Medio-Vasconcelos, B., Slenders, E., Leys, J., Peeters, M., van

1462   Grinsven, B., Gruber, J., Glorieux, C., Pfeiffer, H., Wagner, P., & Thoen, J. (2015). *Phase*

1463   *Transitions of Binary Lipid Mixtures: A Combined Study by Adiabatic Scanning*

1464   *Calorimetry and Quartz Crystal Microbalance with Dissipation Monitoring* [Research

1465   Article]. Advances in Condensed Matter Physics; Hindawi.

1466   https://doi.org/10.1155/2015/479318

1467   Mabrey, S., & Sturtevant, J. M. (1976). Investigation of phase transitions of lipids and lipid

1468   mixtures by high sensitivity differential scanning calorimetry. *Proceedings of the*

1469   *National Academy of Sciences of the United States of America*, *73*(11), 3862–3866.

1470   https://doi.org/10.1073/pnas.73.11.3862

1471   Maeda, N., Senden, T. J., & di Meglio, J.-M. (2002). Micromanipulation of phospholipid bilayers

1472   by atomic force microscopy. *Biochimica et Biophysica Acta (BBA) - Biomembranes*,

1473   *1564*(1), 165–172.

1474   Mannock, D. A., Lewis, R. N. A. H., & McElhaney, R. N. (2010). A calorimetric and spectroscopic

1475   comparison of the effects of ergosterol and cholesterol on the thermotropic phase

1476   behavior and organization of dipalmitoylphosphatidylcholine bilayer membranes.

1477   *Biochimica Et Biophysica Acta*, *1798*(3), 376–388.

1478   https://doi.org/10.1016/j.bbamem.2009.09.002

1479   Marcus, W. D., & Hochmuth, R. M. (2002). Experimental Studies of Membrane Tethers Formed

1480   from Human Neutrophils. *Annals of Biomedical Engineering*, *30*(10), 1273–1280.

1481   https://doi.org/10.1114/1.1528614

1482   Marszalek, P E, Lu, H., Li, H. B., Carrion-Vazquez, M., Oberhauser, A. F., Schulten, K., &

1483   Fernandez, J. M. (1999). Mechanical unfolding intermediates in titin modules. *Nature*,

1484   *402*(6757), 100–103.

1485   Marszalek, Piotr E, Li, H., & Fernandez, J. M. (2001). Fingerprinting polysaccharides with single-

1486   molecule atomic force microscopy. *Nat Biotech*, *19*(3), 258–262.

1487   Mennicke, U., & Salditt, T. (2002). Preparation of solid-supported lipid bilayers by spin-coating.

1488   *Langmuir*, *18*(21), 8172–8177. https://doi.org/10.1021/la025863f

1489   Mierzwa, B. E., Chiaruttini, N., Redondo-Morata, L., von Filseck, J. M., Koenig, J., Larios, J.,

1490   Poser, I., Mueller-Reichert, T., Scheuring, S., Roux, A., & Gerlich, D. W. (2017). Dynamic

1491   subunit turnover in ESCRT-III assemblies is regulated by Vps4 to mediate membrane

1492   remodelling during cytokinesis. *Nature Cell Biology*, *19*(7), 787-+.

1493   https://doi.org/10.1038/ncb3559

1494   Mills, T. T., Huang, J., Feigenson, G. W., & Nagle, J. F. (2009). Effects of cholesterol and

1495   unsaturated DOPC lipid on chain packing of saturated gel-phase DPPC bilayers. *General*

1496   *Physiology and Biophysics*, *28*(2), 126–139.

1497   Mingeot-Leclercq, M. P., Deleu, M., Brasseur, R., & Dufrene, Y. F. (2008). Atomic force

1498   microscopy of supported lipid bilayers. *Nature Protocols*, *3*(10), 1654–1659.

1499   https://doi.org/10.1038/nprot.2008.149

1500   Miyoshi, T., Lönnfors, M., Peter Slotte, J., & Kato, S. (2014). A detailed analysis of partial

1501   molecular volumes in DPPC/cholesterol binary bilayers. *Biochimica Et Biophysica Acta*,

1502   *1838*(12), 3069–3077. https://doi.org/10.1016/j.bbamem.2014.07.004

1503   Morandat, S., Azouzi, S., Beauvais, E., Mastouri, A., & El Kirat, K. (2013). Atomic force

1504   microscopy of model lipid membranes. *Analytical and Bioanalytical Chemistry*, *405*(5),

1505   1445–1461. https://doi.org/10.1007/s00216-012-6383-y

1506   Mouritsen, O. G., & Bloom, M. (1984). MATTRESS MODEL OF LIPID-PROTEIN INTERACTIONS IN

1507   MEMBRANES. *Biophysical Journal*, *46*(2), 141–153.

1508   Nagle, J. F., & Tristram-Nagle, S. (2000). Structure of lipid bilayers. *Biochimica Et Biophysica*

1509   *Acta-Reviews on Biomembranes*, *1469*(3), 159–195. https://doi.org/10.1016/s0304-

1510   4157(00)00016-2

1511   Nawaz, S., Sánchez, P., Schmitt, S., Snaidero, N., Mitkovski, M., Velte, C., Brückner, B. R.,

1512   Alexopoulos, I., Czopka, T., Jung, S. Y., Rhee, J. S., Janshoff, A., Witke, W., Schaap, I. A.

1513   T., Lyons, D. A., & Simons, M. (2015). Actin Filament Turnover Drives Leading Edge

1514   Growth during Myelin Sheath Formation in the Central Nervous System.

1515   *Developmental Cell*, *34*(2), 139–151. https://doi.org/10.1016/j.devcel.2015.05.013

1516   Neupane, S., De Smet, Y., Renner, F. U., & Losada-Pérez, P. (2018). Quartz Crystal Microbalance

1517   With Dissipation Monitoring: A Versatile Tool to Monitor Phase Transitions in

1518   Biomimetic Membranes. *Frontiers in Materials*, *5*.

1519   https://doi.org/10.3389/fmats.2018.00046

1520   Noy, A., Vezenov, D. V, & Lieber, C. M. (1997). CHEMICAL FORCE MICROSCOPY. *Annual Review*

1521   *of Materials Science*, *27*(1), 381–421.

1522   https://doi.org/10.1146/annurev.matsci.27.1.381

1523   Olsson, A. L. J., Quevedo, I. R., He, D., Basnet, M., & Tufenkji, N. (2013). Using the Quartz

1524   Crystal Microbalance with Dissipation Monitoring to Evaluate the Size of Nanoparticles

1525   Deposited on Surfaces. *ACS Nano*, *7*(9), 7833–7843.

1526   https://doi.org/10.1021/nn402758w

1527   Pan, J., Mills, T. T., Tristram-Nagle, S., & Nagle, J. F. (2008). Cholesterol perturbs lipid bilayers

1528   nonuniversally. *Physical Review Letters*, *100*(19), 198103.

1529   https://doi.org/10.1103/PhysRevLett.100.198103

1530   Parot, P., Dufrêne, Y. F., Hinterdorfer, P., Le Grimellec, C., Navajas, D., Pellequer, J. L., &

1531   Scheuring, S. (2007). Past, present and future of atomic force microscopy in life

1532   sciences and medicine. *J Mol Recognit*, *20*(6), 418–431.

1533   https://doi.org/10.1002/jmr.857

1534   Peschel, A., Langhoff, A., Uhl, E., Dathathreyan, A., Haindl, S., Johannsmann, D., & Reviakine, I.

1535   (2016). Lipid phase behavior studied with a quartz crystal microbalance: A technique

1536   for biophysical studies with applications in screening. *The Journal of Chemical Physics*,

1537   *145*(20), 204904. https://doi.org/10.1063/1.4968215

1538   Picas, L., Montero, M. T., Morros, A., Cabanas, M. E., Seantier, B., Milhiet, P.-E., & Hernandez-

1539   Borrell, J. (2009). Calcium-Induced Formation of Subdomains in

1540   Phosphatidylethanolamine-Phosphatidylglycerol Bilayers: A Combined DSC, (31)P

1541   NMR, and AFM Study. *Journal of Physical Chemistry B*, *113*(14), 4648–4655.

1542   https://doi.org/10.1021/jp8102468

1543   Picas, L., Rico, F., & Scheuring, S. (2012). Direct Measurement of the Mechanical Properties of

1544   Lipid Phases in Supported Bilayers. *Biophysical Journal*, *102*(1), L1–L3.

1545   https://doi.org/10.1016/j.bpj.2011.11.4001

1546   Piggot, T. J., Allison, J. R., Sessions, R. B., & Essex, J. W. (2017). On the Calculation of Acyl Chain

1547   Order Parameters from Lipid Simulations. *Journal of Chemical Theory and*

1548   *Computation*, *13*(11), 5683–5696. https://doi.org/10.1021/acs.jctc.7b00643

1549   Pinkwart, K., Schneider, F., Lukoseviciute, M., Sauka-Spengler, T., Lyman, E., Eggeling, C., &

1550   Sezgin, E. (2019). Nanoscale dynamics of cholesterol in the cell membrane. *Journal of*

1551   *Biological Chemistry*, *294*(34), 12599–12609.

1552   https://doi.org/10.1074/jbc.RA119.009683

1553   Pramanik, S. K., Seneca, S., Ethirajan, A., Neupane, S., Renner, F. U., & Losada-Pérez, P. (2016).

1554   Ionic strength dependent vesicle adsorption and phase behavior of anionic

1555   phospholipids on a gold substrate. *Biointerphases*, *11*(1), 019006.

1556   https://doi.org/10.1116/1.4939596

1557   Radmacher, M. (1997). Measuring the elastic properties of biological samples with the AFM.

1558   *IEEE Engineering in Medicine and Biology Magazine*, *16*(2), 47–57.

1559   https://doi.org/10.1109/51.582176

1560   Rascol, E., Devoisselle, J.-M., & Chopineau, J. (2016). The relevance of membrane models to

1561   understand nanoparticles–cell membrane interactions. *Nanoscale*, *8*(9), 4780–4798.

1562   https://doi.org/10.1039/C5NR07954C

1563   Rawicz, W., Olbrich, K. C., McIntosh, T., Needham, D., & Evans, E. (2000). Effect of chain length

1564   and unsaturation on elasticity of lipid bilayers. *Biophysical Journal*, *79*(1), 328–339.

1565   Redondo-Morata, L, Giannotti, M. I., & Sanz, F. (2012a). AFM-Based Force-Clamp Monitors

1566   Lipid Bilayer Failure Kinetics. *Langmuir*, *28*(15), 6403–6410.

1567   https://doi.org/10.1021/la3005147

1568   Redondo-Morata, L, Giannotti, M. I., & Sanz, F. (2012b). Influence of Cholesterol on the Phase

1569   Transition of Lipid Bilayers: A Temperature-Controlled Force Spectroscopy Study.

1570   *Langmuir*, *28*(35), 12851–12860. https://doi.org/10.1021/la302620t

1571   Redondo-Morata, L, Giannotti, M. I., & Sanz, F. (2012c). Influence of Cholesterol on the Phase

1572   Transition of Lipid Bilayers: A Temperature-Controlled Force Spectroscopy Study.

1573   *Langmuir*, *28*(35), 12851–12860. https://doi.org/10.1021/la302620t

1574   Redondo-Morata, L., Giannotti, M. I., & Sanz, F. (2012). Stability of Lipid Bilayers as Model

1575   Membranes: Atomic Force Microscopy and Spectroscopy Approach. In *Atomic Force*

1576   *Microscopy in Liquid: Biological Applications*.

1577   https://doi.org/10.1002/9783527649808.ch10

1578   Redondo-Morata, L, Giannotti, M. I., & Sanz, F. (2014). Structural impact of cations on lipid

1579   bilayer models: Nanomechanical properties by AFM-force spectroscopy. *Molecular*

1580   *Membrane Biology*, *31*(1), 17–28. https://doi.org/10.3109/09687688.2013.868940

1581   Redondo-Morata, L, Sanford, R. L., Andersen, O. S., & Scheuring, S. (2016). Effect of Statins on

1582   the Nanomechanical Properties of Supported Lipid Bilayers. *Biophysical Journal*,

1583   *111*(2), 363–372. https://doi.org/10.1016/j.bpj.2016.06.016

1584   Redondo-Morata, Lorena, Oncins, G., & Sanz, F. (2012). Force Spectroscopy Reveals the Effect

1585   of Different Ions in the Nanomechanical Behavior of Phospholipid Model Membranes:

1586   The Case of Potassium Cation. *Biophysical Journal*, *102*(1), 66–74.

1587   https://doi.org/10.1016/j.bpj.2011.10.051

1588   Reimhult, E., Hook, F., & Kasemo, B. (2003). Intact vesicle adsorption and supported

1589   biomembrane formation from vesicles in solution: Influence of surface chemistry,

1590   vesicle size, temperature, and osmotic pressure. *Langmuir*, *19*(5), 1681–1691.

1591   https://doi.org/10.1021/la0263920

1592   Relat-Goberna, J., Beedle Amy, E. M., & Garcia-Manyes, S. (2017). The Nanomechanics of Lipid

1593   Multibilayer Stacks Exhibits Complex Dynamics. *Small*, *13*(24), 1700147.

1594   https://doi.org/10.1002/smll.201700147

1595   Reviakine, I., Gallego, M., Johannsmann, D., & Tellechea, E. (2012). Adsorbed liposome

1596   deformation studied with quartz crystal microbalance. *The Journal of Chemical Physics*,

1597   *136*(8), 084702. https://doi.org/10.1063/1.3687351

1598   Reviakine, I., Johannsmann, D., & Richter, R. P. (2011). Hearing What You Cannot See and

1599   Visualizing What You Hear: Interpreting Quartz Crystal Microbalance Data from

1600   Solvated Interfaces. *Analytical Chemistry*, *83*(23), 8838–8848.

1601   https://doi.org/10.1021/ac201778h

1602   Richter, R., Mukhopadhyay, A., & Brisson, A. (2003). Pathways of Lipid Vesicle Deposition on

1603   Solid Surfaces: A Combined QCM-D and AFM Study. *Biophysical Journal*, *85*(5), 3035–

1604   3047.

1605   Richter, R P. (2006). Formation of solid-supported lipid bilayers: An integrated view. *Langmuir*,

1606   *22*(8), 3497–3505. https://doi.org/10.1021/la052687c

1607   Richter, Ralf P, & Brisson, A. (2003). Characterization of Lipid Bilayers and Protein Assemblies

1608   Supported on Rough Surfaces by Atomic Force Microscopy. *Langmuir*, *19*(5), 1632–

1609   1640. https://doi.org/10.1021/la026427w

1610   Richter, Ralf P, & Brisson, A. R. (2005). Following the Formation of Supported Lipid Bilayers on

1611   Mica: A Study Combining AFM, QCM-D, and Ellipsometry. *Biophysical Journal*, *88*(5),

1612   3422–3433. https://doi.org/10.1529/biophysj.104.053728

1613   Rief, M., Oesterhelt, F., Heymann, B., & Gaub, H. E. (1997). Single Molecule Force Spectroscopy

1614   on Polysaccharides by Atomic Force Microscopy. *Science*, *275*(5304), 1295 LP – 1297.

1615   https://doi.org/10.1126/science.275.5304.1295

1616   Rog, T., Pasenkiewicz-Gierula, M., Vattulainen, I., & Karttunen, M. (2009). Ordering effects of

1617   cholesterol and its analogues. *Biochimica Et Biophysica Acta-Biomembranes*, *1788*(1),

1618   97–121. https://doi.org/10.1016/j.bbamem.2008.08.022

1619   Roux, A. (2013). The physics of membrane tubes: Soft templates for studying cellular

1620   membranes. *Soft Matter*, *9*(29), 6726–6736.

1621   Sauerbrey, G. (1959). Verwendung von Schwingquarzen zur Wägung dünner Schichten und zur

1622   Mikrowägung. *Zeitschrift für Physik*, *155*(2), 206–222.

1623   https://doi.org/10.1007/BF01337937

1624   Schmidtke, D. W., & Diamond, S. L. (2000). Direct Observation of Membrane Tethers Formed

1625   during Neutrophil Attachment to Platelets or P-Selectin under Physiological Flow. *The*

1626   *Journal of Cell Biology*, *149*(3), 719.

1627   Schneider, J., Dufrene, Y. F., Barger, W. R., & Lee, G. U. (2000). Atomic force microscope image

1628   contrast mechanisms on supported lipid bilayers. *Biophysical Journal*, *79*(2), 1107–

1629   1118.

1630   Sebaaly, C., Greige-Gerges, H., & Charcosset, C. (2019). *Chapter 11—Lipid Membrane Models*

1631   *for Biomembrane Properties' Investigation* (A. Basile & C. B. T.-C. T. and F. D. on (Bio-)

1632   M. Charcosset, Eds.; pp. 311–340). Elsevier. https://doi.org/10.1016/B978-0-12-

1633   813606-5.00011-7

1634   Seeger, H. M., Di Cerbo, A., Alessandrini, A., & Facci, P. (2010). Supported Lipid Bilayers on

1635   Mica and Silicon Oxide: Comparison of the Main Phase Transition Behavior. *Journal of*

1636   *Physical Chemistry B*, *114*(27), 8926–8933. https://doi.org/10.1021/jp1026477

1637   Sessa, G., & Weissmann, G. (1968). Phospholipid spherules (liposomes) as a model for

1638   biological membranes. *Journal of Lipid Research*, *9*(3), 310–318.

1639   Shao, J.-Y., Ting-Beall, H. P., & Hochmuth, R. M. (1998). Static and dynamic lengths of

1640   neutrophil microvilli. *Proceedings of the National Academy of Sciences*, *95*(12), 6797.

1641   Sheetz, M. P. (2001). Cell control by membrane-cytoskeleton adhesion. *Nature Reviews*

1642   *Molecular Cell Biology*, *2*, 392.

1643   Shinoda, K., Shinoda, W., & Mikami, M. (2007). Molecular dynamics simulation of an archaeal

1644   lipid bilayer with sodium chloride. *Physical Chemistry Chemical Physics*, *9*(5), 643–650.

1645   https://doi.org/10.1039/b611543h

1646   Simons, K., & Ikonen, E. (1997). Functional rafts in cell membranes. *Nature*, *387*(6633), 569–

1647   572. https://doi.org/10.1038/42408

1648   Singer, S. J., & Nicolson, G. L. (1972). FLUID MOSAIC MODEL OF STRUCTURE OF CELL-

1649   MEMBRANES. *Science*, *175*(4023), 720-. https://doi.org/10.1126/science.175.4023.720

1650   Siontorou, C. G., Nikoleli, G.-P., Nikolelis, D. P., & Karapetis, S. K. (2017). Artificial Lipid

1651   Membranes: Past, Present, and Future. *Membranes*, *7*(3), 38.

1652   https://doi.org/10.3390/membranes7030038

1653 Steinkühler, J., Sezgin, E., Urbančič, I., Eggeling, C., & Dimova, R. (2019). Mechanical properties

1654 of plasma membrane vesicles correlate with lipid order, viscosity and cell density.

1655 *Communications Biology*, *2*(1), 1–8. https://doi.org/10.1038/s42003-019-0583-3

1656 Strulson, M. K., & Maurer, J. A. (2011). Microcontact printing for creation of patterned lipid

1657 bilayers on tetraethylene glycol self-assembled monolayers. *Langmuir : The ACS*

1658 *Journal of Surfaces and Colloids*, *27*(19), 12052–12057.

1659 https://doi.org/10.1021/la201839w

1660 Sullan, R M A, Li, J. K., Hao, C. C., Walker, G. C., & Zou, S. (2010). Cholesterol-Dependent

1661 Nanomechanical Stability of Phase-Segregated Multicomponent Lipid Bilayers.

1662 *Biophysical Journal*, *99*(2), 507–516. https://doi.org/10.1016/j.bpj.2010.04.044

1663 Sullan, Ruby May A, Li, J. K., & Zou, S. (2009a). Direct Correlation of Structures and

1664 Nanomechanical Properties of Multicomponent Lipid Bilayers. *Langmuir*, *25*(13), 7471–

1665 7477. https://doi.org/10.1021/la900395w

1666 Sullan, Ruby May A, Li, J. K., & Zou, S. (2009b). Quantification of the Nanomechanical Stability

1667 of Ceramide-Enriched Domains. *Langmuir*, *25*(22), 12874–12877.

1668 https://doi.org/10.1021/la903442s

1669 Sun, M., Graham, J. S., Hegedüs, B., Marga, F., Zhang, Y., Forgacs, G., & Grandbois, M. (2005).

1670 Multiple Membrane Tethers Probed by Atomic Force Microscopy. *Biophysical Journal*,

1671 *89*(6), 4320–4329.

1672 Tabaei, S. R., Gillissen, J. J. J., Vafaei, S., Groves, J. T., & Cho, N.-J. (2016). Size-dependent,

1673 stochastic nature of lipid exchange between nano-vesicles and model membranes.

1674 *Nanoscale*, *8*(27), 13513–13520. https://doi.org/10.1039/C6NR03817D

1675 Tellechea, E., Johannsmann, D., Steinmetz, N. F., Richter, R. P., & Reviakine, I. (2009). Model-

1676 Independent Analysis of QCM Data on Colloidal Particle Adsorption. *Langmuir*, *25*(9),

1677 5177–5184. https://doi.org/10.1021/la803912p

1678   Tero, R. (2012). Substrate Effects on the Formation Process, Structure and Physicochemical

1679   Properties of Supported Lipid Bilayers. *Materials*, *5*(12), 2658–2680.

1680   https://doi.org/10.3390/ma5122658

1681   Van Lehn, R. C., Ricci, M., Silva, P. H. J., Andreozzi, P., Reguera, J., Voïtchovsky, K., Stellacci, F.,

1682   & Alexander-Katz, A. (2014). Lipid tail protrusions mediate the insertion of

1683   nanoparticles into model cell membranes. *Nature Communications*, *5*(1), 4482.

1684   https://doi.org/10.1038/ncomms5482

1685   van Meer, G., & de Kroon, A. I. P. M. (2011). Lipid map of the mammalian cell. *Journal of Cell

1686   Science*, *124*(1), 5.

1687   van Meer, G., Voelker, D. R., & Feigenson, G. W. (2008). Membrane lipids: Where they are and

1688   how they behave. *Nature Reviews Molecular Cell Biology*, *9*(2), 112–124.

1689   https://doi.org/10.1038/nrm2330

1690   Veatch, S. L., & Keller, S. L. (2003). Separation of Liquid Phases in Giant Vesicles of Ternary

1691   Mixtures of Phospholipids and Cholesterol. *Biophysical Journal*, *85*(5), 3074–3083.

1692   Vereb, G., Szöllősi, J., Matkó, J., Nagy, P., Farkas, T., Vígh, L., Mátyus, L., Waldmann, T. A., &

1693   Damjanovich, S. (2003). Dynamic, yet structured: The cell membrane three decades

1694   after the Singer–Nicolson model. *Proceedings of the National Academy of Sciences*,

1695   *100*(14), 8053 LP – 8058. https://doi.org/10.1073/pnas.1332550100

1696   Vist, M. R., & Davis, J. H. (1990). Phase equilibria of cholesterol/dipalmitoylphosphatidylcholine

1697   mixtures: Deuterium nuclear magnetic resonance and differential scanning

1698   calorimetry. *Biochemistry*, *29*(2), 451–464. https://doi.org/10.1021/bi00454a021

1699   Vogel, V. (2006). MECHANOTRANSDUCTION INVOLVING MULTIMODULAR PROTEINS:

1700   Converting Force into Biochemical Signals. *Annual Review of Biophysics and

1701   Biomolecular Structure*, *35*(1), 459–488.

1702   https://doi.org/10.1146/annurev.biophys.35.040405.102013

1703   Voinova, M. V., Rodahl, M., Jonson, M., & Kasemo, B. (1999). Viscoelastic Acoustic Response of

1704   Layered Polymer Films at Fluid-Solid Interfaces: Continuum Mechanics Approach.

1705   *Physica Scripta*, *59*(5), 391. https://doi.org/10.1238/Physica.Regular.059a00391

1706   Wallace, E. J., Hooper, N. M., & Olmsted, P. D. (2006). Effect of hydrophobic mismatch on

1707   phase behavior of lipid membranes. *Biophysical Journal*, *90*(11), 4104–4118.

1708   https://doi.org/10.1529/biophysj.105.062778

1709   Wargenau, A., & Tufenkji, N. (2014). Direct Detection of the Gel–Fluid Phase Transition of a

1710   Single Supported Phospholipid Bilayer Using Quartz Crystal Microbalance with

1711   Dissipation Monitoring. *Analytical Chemistry*, *86*(16), 8017–8020.

1712   https://doi.org/10.1021/ac5019183

1713   Winkler, P. M., Campelo, F., Giannotti, M. I., & García-Parajo, M. F. (2020). Planar plasmonic

1714   antenna arrays resolve transient nanoscopic heterogeneities in biological membranes.

1715   *Proc.SPIE*, *11246*. https://doi.org/10.1117/12.2543726

1716   Winkler, P. M., Regmi, R., Flauraud, V., Brugger, J., Rigneault, H., Wenger, J., & García-Parajo,

1717   M. F. (2017). Transient Nanoscopic Phase Separation in Biological Lipid Membranes

1718   Resolved by Planar Plasmonic Antennas. *ACS Nano*, *11*(7), 7241–7250.

1719   https://doi.org/10.1021/acsnano.7b03177

1720   Yeagle, P. L. (1989). Lipid regulation of cell membrane structure and function. *The FASEB*

1721   *Journal*, *3*(7), 1833–1842. https://doi.org/10.1096/fasebj.3.7.2469614

1722   Zou, S., & Johnston, L. J. (2010). Ceramide-enriched microdomains in planar membranes.

1723   *Current Opinion in Colloid & Interface Science*, *15*(6), 489–498.

1724   https://doi.org/10.1016/j.cocis.2010.06.003

1725

1726

1727

1728

1729